

## Review

## A review on microstructural study and compressive strength of geopolymer mortar, paste and concrete

Connie Ng<sup>a</sup>, U. Johnson Alengaram<sup>a,\*</sup>, Leong Sing Wong<sup>b</sup>, Kim Hung Mo<sup>a</sup>, Mohd Zamin Jumaat<sup>a</sup>, S. Ramesh<sup>c</sup>

<sup>a</sup> Centre for Innovative Construction Technology (CICT), Department of Civil Engineering, Faculty of Engineering, University of Malaya, 50603 Kuala Lumpur, Malaysia

<sup>b</sup> College of Graduate Studies, Universiti Tenaga Nasional, Jalan Ikram-Uniten, 43000 Kajang, Selangor, Malaysia

<sup>c</sup> Department of Mechanical Engineering, Faculty of Engineering, University of Malaya, 50603 Kuala Lumpur, Malaysia

## HIGHLIGHTS

- Compressive strength characteristics analysed using microstructural investigation.
- Binders mixed with lower mass ratio of SS/SH tend to react more efficiently.
- Evaporation of free water molecule causes weight loss in the specimen.
- Nano materials in binders with low pozzolanic oxide content is important to form Si—O—Al—O bond.

## ARTICLE INFO

## Article history:

Received 11 February 2018

Received in revised form 21 June 2018

Accepted 11 July 2018

## Keywords:

Geopolymer paste and mortar

Microstructure

Compressive strength

Aluminosilicate

Alkali activator

Microcracks

## ABSTRACT

The utmost priority in reducing the usage of ordinary Portland cement (OPC) while replicating the cementitious properties by utilizing industrial by-products in construction materials is seriously undertaken by many researchers. The technology of geopolymerization that utilizes materials and activator solution to form geopolymer matrix could lead to alleviate some of the issues related to OPC based concrete. Numerous experiments have established that geopolymer concrete has higher compressive strength, higher acid resistivity and lower shrinkage than ordinary concrete. This review article focusses on the microstructure analyses of the geopolymer specimens and comparison of geopolymers with various binders. The review analysis of various binders used and their microstructural investigations reveal that different molarity of sodium hydroxide or phosphoric acid solution, liquid-to-binder ratio, curing temperature and duration yield geopolymers of diverse properties. Most of the geopolymer products revealed a wide hump in the XRD analysis due to the amorphous structure of aluminosilicate. Investigation of MIP and Micro CT reveals that aged geopolymer has a denser matrix arrangement and produce high compressive strength. Geopolymerization prevents interconnectivity of micropores due to the formation of denser matrix of geopolymer gel. Generally, the use of 12M of sodium hydroxide solution, low liquid-to-binder ratio of about 0.4 and curing temperature at approximately 70 °C for at least 24 h produced high strength geopolymers. The binders mixed with lower sodium silicate to sodium hydroxide mass ratio of 2.0–2.5 tend to react more efficiently.

© 2018 Elsevier Ltd. All rights reserved.

## Contents

1. Introduction .....	551
2. Geopolymerization .....	551
3. Review of literature .....	553
3.1. Chemical composition of binder materials .....	553
3.2. Mixes and compressive strengths of geopolymer .....	553
3.3. Microstructure of geopolymers .....	554
3.3.1. Scanning electron microscopy (SEM) of geopolymers .....	554

\* Corresponding author.

E-mail address: [johnson@um.edu.my](mailto:johnson@um.edu.my) (U.J. Alengaram).

3.3.2.	X-ray diffraction (XRD) of geopolymers .....	563
3.3.3.	Fourier transform infrared spectroscopy (FTIR) .....	567
3.3.4.	Thermogravimetric analysis.....	572
3.3.5.	Mercury intrusion porosimetry .....	573
3.3.6.	Micro computed tomography analysis .....	573
4.	Conclusion .....	574
	Conflict of interest.....	575
	Acknowledgments .....	575
	References .....	575

## 1. Introduction

It is well known that limestone hills were being harvested for cement manufacturing throughout the world and that lead to ecological imbalance [1]. As concrete is the most widely used construction material, the exploitation of natural resources such as sand and coarse aggregate pressured construction industry to look for alternatives for these materials; thus, the use of alternative construction materials is on the rise and many research works are being carried out through the globe.

Cement manufacturers rely on limestone as it is the major source in ordinary Portland cement. For the conversion of limestone to calcium oxide, the cement kiln heats all the raw materials at high temperature. Fuel used in heating may be coal, natural gas, sawdust and methane gas or a combination of these fuels. Both the chemical conversion and firing process release carbon dioxide (CO<sub>2</sub>), which is the main component in greenhouse gas. Alnahhal et al. [2] reported that about 2.8 billion tonnes of cement products manufactured every year and this in turn produces about 5–7% of the global CO<sub>2</sub> emissions [3,4]. Based on a report by Department of Statistic Malaysia, roughly 20 Mega tonnes of cement were produced in 2016 [5]. It has been reported that the production of cement, besides consuming the natural resources, it also destroys the natural habitat of flora and fauna [1]. Since the beginning of 1990s, the term sustainability has gained significance among all engineering community and more focused works are being systematically carried out throughout the globe in diverse areas of engineering process and products. Thus, more researches have been carried out in the area of building materials, especially on cement-based products by using diverse cement replacement materials which fulfill both the sustainability criterion to conserve the natural resources and preserve the environment.

The production of industrial by-products and waste is increasing rapidly due to unrestrained and fast-growing industrialization & urbanization and some of these could be converted into potential raw materials for building products. One such material that has long been researched is ash that could partially replace cement. The enormous amount of industrial waste ash produced from power generation, timber manufacturing, iron and steel, rice mill, mining industries, etc. posed a great environmental threat as its disposal causes serious concern to environment and health. Some of the industrial by-products and wastes that have been researched include fly ash, bottom ash, silica fume, boiler slag, steel slag, palm oil fuel ash, rice husk ash and fluidized bed combustion ash. In Southeast Asia, the use of coal as fuel in coal power plants and the production of vast amount of rice result in the production of fly ash, bottom ash and rice husk ash. In Malaysia, fly ash and bottom ash are categorized as schedule wastes by the Department of Environment (DOE). DOE of Malaysia does not allow any of the waste ash to be released into sanitary landfills due to its high concentration in toxicity [6]. Thus, this explains that large dump yard is required for the power plant to store the waste ashes.

On the other hand, recent trend on replacement of cement by alkali activated materials and geopolymer concrete opened up

new avenue for researchers throughout the globe to embark on utilizing potential waste ashes into commercial entity. Previous studies have shown that geopolymer concrete has high compressive strength, effective in acid resistance, lower shrinkage and effective in heavy metal absorption compared with concrete made with Portland cement [7–12]. Studies also revealed that geopolymer is capable in reducing the power consumption up to 15% for stabilizing indoor temperature [13]. Geopolymers are made up of aluminosilicate materials with three-dimensional amorphous microstructure. Geopolymerization process takes place when the oxides of silicon and aluminium minerals or aluminosilicates are activated by alkaline solution. Materials that are rich in aluminosilicates are calcined kaolinite and industrial waste such as fly ash, bottom ash and rice husk ash are activated by adding sodium hydroxide, sodium silicate, potassium hydroxide or potassium silicate. While the industrial waste ashes are reutilized for geopolymer production, the amount of greenhouse gas emitted to the environment was lowered by 44–64% compared with the production of Portland cement [14]. This is attributed to ambient temperature without external heating of geopolymers that achieve the desired strength in such curing condition.

Research interest in geopolymer concrete and the application has been displayed at the University of Queensland's Global Change Institute (GCI) built in Australia [15]. Combination of slag and FA were used to develop the geopolymer concrete for the construction of CGI; there are other binders studied such as metakaolin, and rice husk ash. OPC has numerous publications expertise in microstructural behavior. However, very limited articles emphasized the microstructural study for GPC.

Thus, this paper aims to present an overview of recent studies of incorporation of waste ashes such as fly ash, bottom ash, palm oil fuel ash, ground granulated blast furnace slag (GGBS) and metakaolin in geopolymers; the investigation on microstructural investigation and its relationship to compressive strength is also reviewed and reported. This review article reiterates the chemical process of geopolymerization and highlights the differences of geopolymers due to materials' chemical composition through scanning electron microscopy (SEM), x-ray diffraction (XRD), x-ray fluorescent (XRF), Fourier transform infrared spectroscopy (FTIR), thermal gravity analysis (TGA), mercury intrusion porosimetry (MIP) and micro computed tomography (Micro CT) analyses.

## 2. Geopolymerization

In 1978, the term 'geopolymer' is introduced by Davidovits (1991) by producing inorganic polymeric materials [16]. Geopolymers are made up of aluminosilicate materials with three-dimensional amorphous microstructure. Alkaline medium (Na<sup>+</sup>, K<sup>+</sup>, Li<sup>+</sup>, Ca<sup>+</sup>, etc.) or acidic medium such as phosphoric acid or humic acid can be used to synthesize geopolymer. In alkaline medium, geopolymerization process takes place when the oxides of silicon and aluminium minerals or aluminosilicates reacts with alkaline solution to form a polymeric Si—O—Al bonds. The structures are of Poly(sialate) type (—Si—O—Al—O—), Poly(sialate-siloxo) type

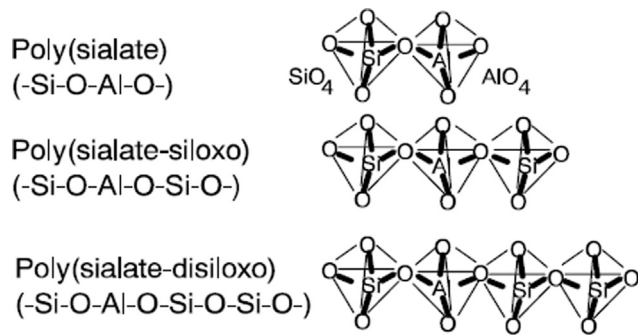
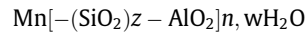


Fig. 1. Graphics of Poly(sialate) [17].

(-Si-O-Al-O-Si-O-) and Poly(sialate-disiloxo) type (-Si-O-Al-O-Si-O-Si-O-) as shown in Fig. 1 [16]. Sialate is an abbreviation used to represent silicon-oxo-aluminate. A network of sialate composed of silicate (SiO<sub>4</sub>) and aluminate (AlO<sub>4</sub>) which is connected tetrahedrally by sharing the oxygen atom. Positives ions is required in the framework cavities in order to equate the negative charge of aluminium ion in IV-fold coordination. The empirical formula of Poly(sialates) is as follow:



where

M is a cation (Na<sup>+</sup>, K<sup>+</sup>, Ca<sup>2+</sup>)

n is the degree of polycondensation

z is 1, 2, 3

Table 1  
Oxide composition for various binder materials.

Materials <sup>a</sup>	Composition (%)															
	SiO <sub>2</sub>	Al <sub>2</sub> O <sub>3</sub>	Fe <sub>2</sub> O <sub>3</sub>	∑ P <sup>b</sup>	CaO	P <sub>2</sub> O <sub>5</sub>	Na <sub>2</sub> O	K <sub>2</sub> O	MnO	MgO	SO <sub>3</sub>	TiO <sub>2</sub>	SrO	Cl	CuO	LOI
OPC [10]	19.01	4.68	3.20	26.89	66.89	0.08	0.09	1.17	0.19	0.81	3.00	-	-	-	-	2.48
FA [11]	61.89	28.05	4.11	94.05	0.87	-	0.40	0.82	-	0.38	1.32	-	-	-	-	0.49
FA [18]	48.80	27.00	10.20	86.00	6.20	1.20	0.37	0.85	0.15	1.40	0.22	1.30	0.16	-	-	1.70
FA [10]	50.70	28.80	8.80	88.30	2.38	-	0.84	2.40	-	1.39	0.30	-	-	-	-	3.79
FA [19]	49.00	31.00	3.00	83.00	5.00	1.00	4.00	1.00	-	3.00	0.00	2.00	-	-	-	0.00
FA [7]	53.50	28.80	7.47	89.77	1.55	-	-	-	-	0.81	0.14	-	-	-	-	3.11
FA [20]	26.40	9.25	30.13	65.78	21.60	0.67	-	2.58	0.27	-	1.30	3.07	-	-	-	3.02
FA [21]	17.57	36.37	12.43	66.37	10.58	-	-	1.77	-	3.05	1.39	0.88	-	-	-	1.19
FA [22]	64.97	26.64	5.69	97.30	0.33	-	0.49	0.25	-	0.85	0.33	-	-	-	-	0.45
FA [23]	27.35	50.85	2.01	80.21	5.41	-	0.04	0.33	0.02	0.28	-	2.12	-	-	-	7.74
FA [24]	54.72	27.28	5.15	87.15	5.31	1.12	0.43	1.00	0.10	1.10	1.01	1.82	0.36	-	0.01	6.80
FA [25]	57.60	28.90	5.80	92.30	0.20	-	-	0.90	-	0.90	0.20	-	-	-	-	3.60
FA [26]	50.67	18.96	6.35	75.98	14.14	-	0.69	-	-	3.12	0.74	-	-	-	-	0.17
FA [27]	66.56	22.47	3.54	92.57	1.64	-	0.58	1.75	-	0.65	0.10	0.88	-	-	-	1.66
FA [28]	63.13	24.88	3.07	91.08	2.58	0.17	0.71	2.01	0.05	0.61	0.18	0.96	-	-	-	1.45
FA [29]	47.87	28.00	14.09	89.96	3.81	1.81	0.41	0.62	0.21	0.93	0.27	1.99	-	-	-	0.43
FA [30]	51.10	25.70	12.50	89.30	4.30	0.90	0.80	0.70	0.20	1.50	0.20	1.30	-	-	-	0.60
FA [31]	52.75	18.05	5.92	76.72	12.92	-	1.11	2.09	0.14	3.86	1.76	1.01	-	-	-	1.60
FA [32]	54.48	27.72	8.14	90.34	1.29	-	0.67	-	-	-	0.11	-	-	-	-	4.11
FA [33]	35.86	15.05	17.31	68.22	17.16	0.30	1.58	3.12	-	2.34	5.94	-	-	-	-	0.10
FA [34]	58.40	23.80	4.19	86.39	7.32	-	1.43	1.02	-	1.11	0.44	-	-	-	-	0.50
FA [35]	50.83	23.15	6.82	80.80	6.87	1.14	1.29	2.14	-	1.70	1.24	1.01	0.19	-	-	0.55
SF [10]	93.67	0.83	1.30	95.80	0.31	-	0.40	1.10	0.84	0.84	0.16	-	-	-	-	2.10
Kaolin [36]	45.30	38.38	0.30	83.98	0.05	-	0.27	0.44	-	0.25	-	-	-	-	-	13.97
Kaolin [37]	41.46	31.47	0.15	73.08	7.65	0.09	0.69	0.51	0.06	0.65	-	1.50	-	-	-	15.76
Kaolinite [38]	45.14	33.32	11.99	90.45	4.13	0.56	0.07	0.13	0.23	1.37	0.48	2.19	-	-	-	0.41
BA [19]	54.00	25.00	4.00	83.00	5.00	1.00	3.00	1.00	-	2.00	0.00	3.00	-	-	-	2.00
POFA [39]	64.17	3.73	6.33	74.23	5.80	5.18	0.18	8.25	0.18	4.87	0.72	0.19	0.02	-	0.08	16.30
POFA [25]	63.40	5.50	5.80	74.70	4.30	-	-	6.30	-	3.70	0.90	-	-	-	-	6.00
POFA [40]	63.41	5.55	4.19	73.15	4.34	3.78	0.16	6.33	0.17	3.74	0.91	0.33	0.02	0.45	6.54	6.20
POFA [41]	43.60	11.40	4.70	59.70	8.40	-	0.39	3.50	-	4.80	2.80	-	-	-	-	18.00
GGBS [27]	32.52	13.70	0.76	46.98	45.83	0.04	0.25	0.48	0.35	3.27	1.80	0.73	0.08	0.02	-	0.60
GGBS [40]	31.52	12.22	1.14	44.88	44.53	-	0.21	0.33	-	4.62	3.24	1.03	-	-	-	0.79
GGBS [42]	33.54	1.17	12.52	47.23	37.93	-	-	-	0.57	9.29	2.51	0.95	-	-	-	1.25
GGBS [35]	34.51	10.30	0.60	45.41	42.84	0.02	0.40	0.52	-	7.41	1.95	0.67	0.05	-	-	0.43
IOT [8]	34.72	16.22	12.31	63.25	7.63	-	0.54	1.52	0.13	8.92	-	0.30	-	-	-	13.18
BOT [42]	32.24	8.67	37.39	78.30	3.15	-	0.85	-	-	0.85	-	2.31	-	-	-	13.74
CP [33]	70.30	1.90	0.42	72.62	12.30	-	12.80	0.23	-	1.68	0.07	-	-	-	-	0.68
FP [33]	68.80	2.40	0.11	71.31	7.43	0.64	15.18	1.42	-	2.70	0.19	-	-	-	-	0.66
Sepiolite [43]	36.15	0.76	0.42	37.33	25.03	-	0.44	0.38	0.02	17.14	-	0.03	-	-	-	19.57
MK [44]	51.70	40.60	0.64	92.94	0.71	0.20	0.31	2.00	0.08	0.96	0.10	3.00	0.03	-	-	1.19
MK [43]	53.32	42.09	2.33	97.74	0.09	-	0.49	0.64	0.02	0.21	-	0.63	-	-	-	0.08
MK [45]	52.14	41.88	1.35	95.37	0.42	-	-	1.10	-	0.38	-	1.30	-	-	-	1.10
CG [45]	53.77	42.75	1.25	97.77	0.10	-	-	0.60	-	0.16	-	1.37	-	-	-	0.09
VA [46]	46.28	15.41	13.32	75.01	9.07	0.63	3.88	1.42	0.19	6.74	-	2.84	-	-	-	0.40
WTS [47]	58.99	24.64	6.63	90.26	0.69	-	4.08	1.54	-	1.14	-	0.88	-	-	-	1.41
WCB [48]	66.15	15.36	5.98	87.49	2.95	-	0.89	2.77	-	2.13	0.11	-	-	-	-	1.50
RHA [44]	93.46	0.58	0.52	94.56	1.03	1.60	0.08	1.82	-	0.51	0.60	-	-	-	-	7.76
RHA [47]	89.17	-	0.41	89.58	0.61	-	7.29	1.12	-	1.22	-	0.03	-	-	-	0.15

<sup>a</sup> Materials: OPC: Ordinary Portland Cement; FA: Fly ash; SF: Silica fume; MK: Metakaolin; IOT: Iron ore tailing; RHA: Rice husk ash; POFA: Palm oil fuel ash; BA: Bottom ash; VA: Volcanic ash; GGBS: Ground granulated blast furnace; CG: Ceramic grog; WTS: Water treatment sludge; CP: Container glass; FP: Fluorescent lamp glass; WCB: Waste clay brick; BOT: Bauxite ore tailing.

<sup>b</sup> ∑ P = Sum of pozzolanic oxide (SiO<sub>2</sub>, Al<sub>2</sub>O<sub>3</sub> and Fe<sub>2</sub>O<sub>3</sub>).

### 3. Review of literature

#### 3.1. Chemical composition of binder materials

X-ray fluorescent (XRF) analysis was carried out to determine the chemical composition of various binders used in the study of geopolymer as shown in Table 1 and the comparison among the chemical composition of binders can be seen. Materials such as fly ash, bottom ash, silica fume, rice husk ash and others have shown fair amount of silica and alumina content, which is suitable to be substitute as supplementary cementitious materials. The major oxides present in most of the fly ash samples were mostly silicon oxide and aluminium oxide. Due to the fact that OPC was processed from limestone, it has a higher content in calcium oxide and silicon oxide but lower in aluminium oxide. As stated in ASTM C-618, ashes can be categorized into class N, F and C based on the pozzolanic oxides, namely SiO<sub>2</sub>, Al<sub>2</sub>O<sub>3</sub> and Fe<sub>2</sub>O<sub>3</sub>. According to the listed previous studies, only GGBS and sepiolite contain less than 50% of pozzolanic oxides. In general, FA studied in previous works fall in class F, which has at least 70% of pozzolanic oxides except for Abdulkareem et al. [20] and Embong et al. [21] Both studies used FA sourced from Manjung power plant, Malaysia which is categorized in class C.

#### 3.2. Mixes and compressive strengths of geopolymer

A number of studies on geopolymer pastes have been carried out in recent years [9,23,49]. Most of the previous researchers used FA as the main binder material, while some studies replaced fly ash partially by using other aluminosilicate-rich materials. The compatibilities of material to bind with FA such as metakaolin, saw dust, iron ore tailing, rice husk ash, POFA and coir fiber were studied.

Recent studies as listed in Tables 2 and 3 show the use of sodium hydroxide and sodium silicate as the main alkali activator, except for a study conducted by Tchakouté & Rüscher [37] where a comparison of acid and alkali medium was reported. Most of the researchers used the activator solution with the molarity range between 8 and 14, except Huiskes et al. [31] who used 3 molarity. The curing temperatures of the studies reviewed ranged from 20 °C to 100 °C. The specimens with low mass ratio of sodium oxide-to-silica tends to expand upon thermal curing [50]. Thus, curing specimens at below 70 °C is beneficial to strength gain while reducing the expansion. The compressive strength for the ceramic grog mixed with metakaolin-based geopolymer mortar after curing for 22 °C for 24 h and ambient temperature for 27 days was 97 MPa. The liquid-to-binder (L/B) ratio is 0.80.

Nimwinya [47] reported that geopolymer paste made with water treatment sludge and rice husk ash has a density of 1300 kg/m<sup>3</sup>, which is the lightest among

**Table 2**  
Compressive strength for various geopolymer paste and mortar.

Author	Type	Material	Density (kg/m <sup>3</sup> )	Molarity (M)	Comp. strength (MPa)	L/B ratio	Curing time & temp.
[49]	Paste	FA	N/A	12	65.0	0.60	60 °C for 1 day
[9]	Paste	Fluidized bed FA-MK	N/A	10	72.0	0.40	40 °C for 1 day
[23]	Paste	Nano TiO <sub>2</sub> in fluidized bed FA-MK	N/A	10	77.0	0.50	40 °C for 3 days
[53]	Paste	FA and SD	1580	10	67.0	0.90	40 °C for 1 day
[8]	Paste	FA and IOT	N/A	10	36.0	0.50	7 thermal cycle at 200 °C
[47]	Paste	RHA and WTS	1300	10	24.0	1.00	60 °C for 1 day
[54]	Paste	FA and coir fiber	N/A	8	31.4	N/A	75 °C for 1 day
[43]	Paste	FA-MK-Sepiolite	N/A	10	52.0	0.45	20 °C for 1 day
[25]	Paste	FA and POFA	1840	14	72.7	0.55	65 °C for 2 days
[45]	Mortar	MK with CG	N/A	N/A	97.0	0.80	22 °C for 1 day
[44]	Mortar	GGBS, MK and RHA	2070	14	47.9	0.50	65 °C for 1 day
[55]	Mortar	FA	1770	16	56.0	0.50	65 °C for 1 day
[32]	Mortar	FA	N/A	14	80.0	–	75 °C for 22 h
[42]	Mortar	BOT and slag	N/A	–	50.0	0.50	95 °C for 1 day

**Table 3**  
Compressive strength for various geopolymer concrete.

Authors	Materials <sup>a</sup>	Density (kg/m <sup>3</sup> )	Molarity (M) (NaOH) <sup>b</sup>	Slump (mm)	Comp. strength (MPa) <sup>c</sup>	L/B ratio	SS/SH ratio <sup>d</sup>	Duration of curing & temperature
[38]	FA	N/A	12	N/A	62.30	0.28	2.50	75 °C for 1 day
[29]	FA	2185	15	735	48.7	0.37	4.50	80 °C for 1 day
[11]	FA	N/A	16	35	53.56	0.21	1.50	60 °C for 1 day
[19]	FA	2372	14	140	34.30	0.30	2.50	25 °C for 1 day
	BA	2035	14	150	0.60	0.50	2.50	25 °C for 1 day
	FA and BA	2345	14	165	8.40	0.50	2.50	25 °C for 1 day
[26]	FA	N/A	14	N/A	42.50	N/A	2.00	46 °C for 1 day
	FA and CR	N/A	14	N/A	40.60	N/A	2.00	46 °C for 1 day
[20]	FA and LWA	1438.7	12	95	17.00	0.60	1.00	70 °C for 1 day
[36]	FA and Kaolin	N/A	14	N/A	54	0.20	2.50	100 °C for 3 days
[10]	FA and SF	N/A	14	150	51.2	0.20	2.50	100 °C for 3 days
[22]	FA and nano silica	N/A	12	120	46.43	0.40	1.75	25 °C for 1 day
[28]	FA and nano silica	2100	8	N/A	47	0.75	2.50	80 °C for 1 day
[21]	FA and LS	N/A	8	N/A	32	0.40	2.50	60 °C for 1 day
[27]	FA and GGBS	2610	12	200+	53.2	0.28	2.50	75 °C for 18 h
[30]	FA with SSD	N/A	8	N/A	62 (7 days curing)	0.35	2.50	60 °C for 1 day
[25]	FA, POFA and OPS	1721	14	N/A	30.1	0.55	2.50	65 °C for 2 days
[31]	PCFA, GGBS and LWA	710	3	250	9.00	0.30	N/A	20 °C for 1 day
[56]	POFA, MK, OPS and steel fiber	1815	14	0	31.9	0.50	2.50	65 °C for 2 days
[40]	POFA, GGBS and MK	2100	14	45	41.5	0.25	2.50	65 °C for 1 day
[37]	MK (Alkali medium)	N/A	N/A	N/A	63.8	0.80	1.50	60 °C for 1 day
	MK (Acid medium)	N/A	10 (H <sub>3</sub> PO <sub>4</sub> )	N/A	93.8	0.80	N/A	60 °C for 1 day

<sup>a</sup> Types of material: FA: Fly ash; MK: Metakaolin; SD: Saw dust; IOT: Iron ore tailing; WTS: Water treatment sludge; RHA: Rice husk ash; POFA: Palm oil fuel ash; LWA: Light weight aggregate; BA: Bottom ash; GGBS: Ground granulated blast furnace; VA: Volcanic ash; CR: Crumb rubber; OPS: Oil palm shell; LS: Limestone; SSD: Saturated surface dry; CG: Ceramic grog; SF: Silica fume; PCFA: Powder coal fly ash; N/A: Not available.

<sup>b</sup> All samples used NaOH, unless otherwise stated.

<sup>c</sup> All samples were tested after 28 days of curing, unless otherwise stated.

<sup>d</sup> SS/SH ratio: Ratio of sodium silicate to sodium hydroxide.

the geopolymer pastes reviewed. On the other hand, fly ash based geopolymer paste investigated by Abdulkareem and Ramli [51] with a mass ratio of SS/SH of 1:1 produced the densest mix of about 1936 kg/m<sup>3</sup>.

Duan et al. [8,23,53] researched on mortar prepared using nano TiO<sub>2</sub> in fluidized bed fly ash with metakaolin; the specimens were cured at 40 °C for 3 days and ambient temperature thereafter obtained 28-day compressive strength of 77 MPa. The L/B ratio used in this study was 0.5. It is understood that higher L/B ratio will lead to lower compressive strength due to the evaporation of free water molecules as confirmed through SEM analysis. With adequate amount of water released from the aluminosilicate matrix, the geopolymerization process will be able to take place effectively [52].

Based on the published data, a graph as shown in Fig. 2 was drawn to highlight the materials used, ratio of sodium silicate/sodium hydroxide (SS/SH) and the compressive strength. It is understood that most of the studies maintained the SS/SH ratio at 2.50. Majority of the researchers investigated FA as sole binder or blended with other binding materials; with the minimum strength of 34 MPa for a FA-based geopolymer. It is necessary to understand that extra binder materials such as kaolin, ground granulated blast furnace slag (GGBS), silica fume and nano silica can be used to enhance the mechanical properties of the geopolymer.

### 3.3. Microstructure of geopolymers

#### 3.3.1. Scanning electron microscopy (SEM) of geopolymers

**3.3.1.1. Fly ash-based geopolymer.** Many researchers reported on fly ash-based geopolymer concrete with variables that include additional binders, alkali activator ratio, molarity, and curing temperature & duration [7,11,19]. Pavithra et al. [11] researched on fly ash-based geopolymer concrete and suggested a method as explained here to obtain optimum mix design. A few parameters such as molarity, SS/SH ratio, curing temperature and duration were set as constant variables before deciding for the alkaline activator solution (AAS). In this study, the authors suggested that water content to be used relied on the maximum aggregate size, as it can be used to control the limit of maximum water content. Calculation on binder content, AAS, water content, fine and coarse aggregate were carried out based on the priority of the mix whether strength or AAS to binder ratio is to be focused on. The effect of different alkaline solution-to-binder contents on microstructure of geopolymer concrete was compared and illustrated in Fig. 3. The precipitation decreases constantly as the ratio of AAS/binder increases. It is understood that as this ratio increases, the strength of geopolymer concrete decreases due to the increasing amount of water present in the geopolymer mix. This phenomenon is comparable with OPC concretes with higher water/cement ratio. The contact area for the reaction was blocked by the water molecules and this in turn affected geopolymerization process between the binder and the activator; this resulted in low compressive strength of geopolymer concrete [57]. With appropriate alkali

activator/binder ratios of 0.4 and 0.5, the unreacted FA particles was found minimum as shown in Fig. 3(a) and (b). In addition, the number of voids is also sparse as shown in Fig. 3(c)–(e). The fineness of fly ash also contributed to the dense matrix, which is helpful in reducing the formation of microcracks. Apart from that, the strength of geopolymers was improved fairly due to the ability of fly ash to fill the microcracks, which is in line with the study of Xie and Ozbakkaloglu [19] and Assi et al. [7].

The effect of different mass ratios of SS/SH of fly ash-based geopolymer was studied through micro-structural investigation by Abdulkareem and Ramli [51]. As illustrated in Fig. 4(a) and (b), fully reacted fly ash was observed for geopolymer with alkaline activator mass ratios of 0.5 and 1.0. Even though similar microstructure was observed for both mass ratios of 0.5 and 1.0, the compressive strength obtained for mass ratio of 1.0 was 65 MPa compared to 35 MPa for mass ratio of 0.5. Supported by previous study, higher concentration of silicate might contribute in higher strength development due to more silicates available for the geopolymerization [58]. However, the comparison of Fig. 4(a and b) with (c and d) shows that higher mass ratio of sodium silicate resulted in unreacted fly ash particles. The use of activator mass ratios of 2.0 and 3.0 displayed high content of unreacted and partially reacted fly ash microspheres. It is understood that too much of AAS in the mix hampered the process of geopolymerization by limiting the interaction between the binder and AAS [59]. Besides, geopolymer samples with SS/SH mass ratio of 3.0 recorded the weakest compressive strength of 32 MPa. The comparison of recent studies on this subject shows that most of the authors used the mass ratio of SS/SH up to 2.5 [10,19,36,38]. While other study has produced similar properties of geopolymer with higher mass ratio of alkaline solution, the curing temperature might have been contributed to the dense structure [29]. Curing temperature of 70 °C or higher tends to have looser arrangement due to evaporation of free water which causes continuous microcracks within the matrix [18,49,60]. According to Chindaprasirt et al. [60], adequate amount of water is necessary for the process of geopolymerization in order to have high strength development.

Okoye et al. [10] examined the microstructure of geopolymer made of fly ash and silica fume. In contrast with previous studies, geopolymer concrete sample with fly ash was found to have fracture surface. The observation of voids proved loose arrangement of particles. Whereas smoother surface was observed for the 20% replacement of fly ash with silica fume in the fly ash-based geopolymer concrete (see Fig. 5).

Fig. 6(a)–(c) show SEM images of pure geopolymer and geopolymer nanocomposites containing 3.0 wt% nano silica in wet and dry mix conditions. As illustrated in Fig. 6(a), significant amount of unreacted and partially reacted fly ash particles was observed in the case of pure geopolymer. However, it is obvious that number of unreacted particles decreased as evidenced in Fig. 6(b) and (c). Besides, microcracks observed using dry mix procedure is lower than the pure geopolymer and wet mix.

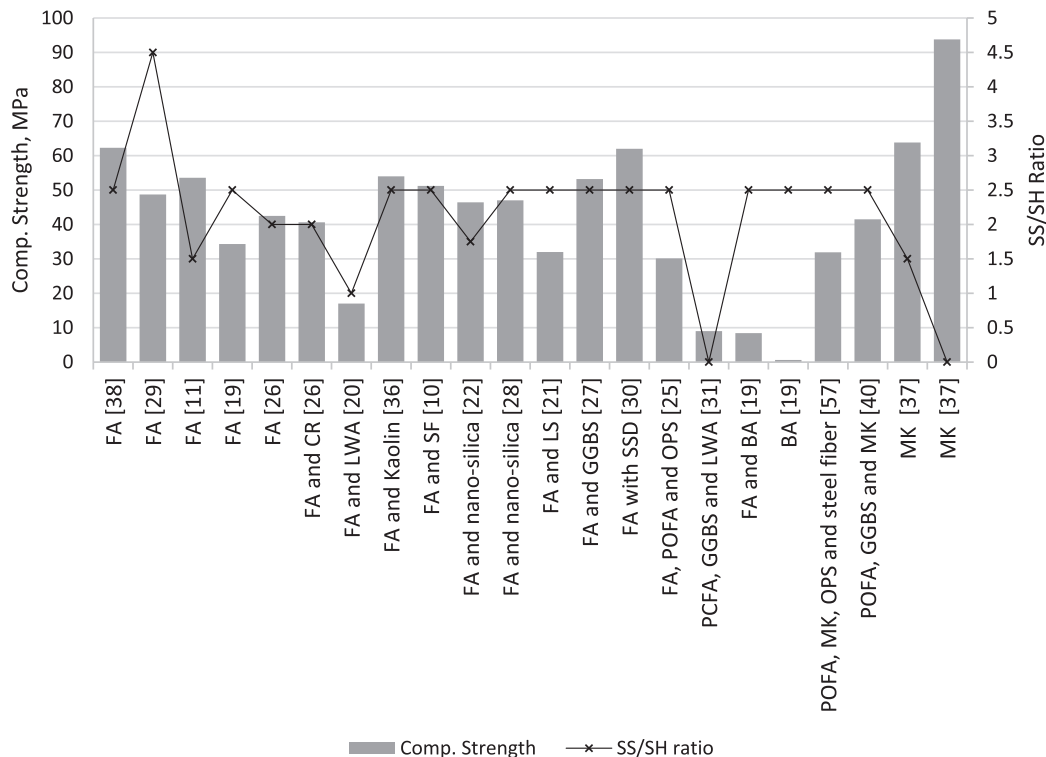


Fig. 2. Comparison of SS/SH ratio with compressive strength for respective studies.

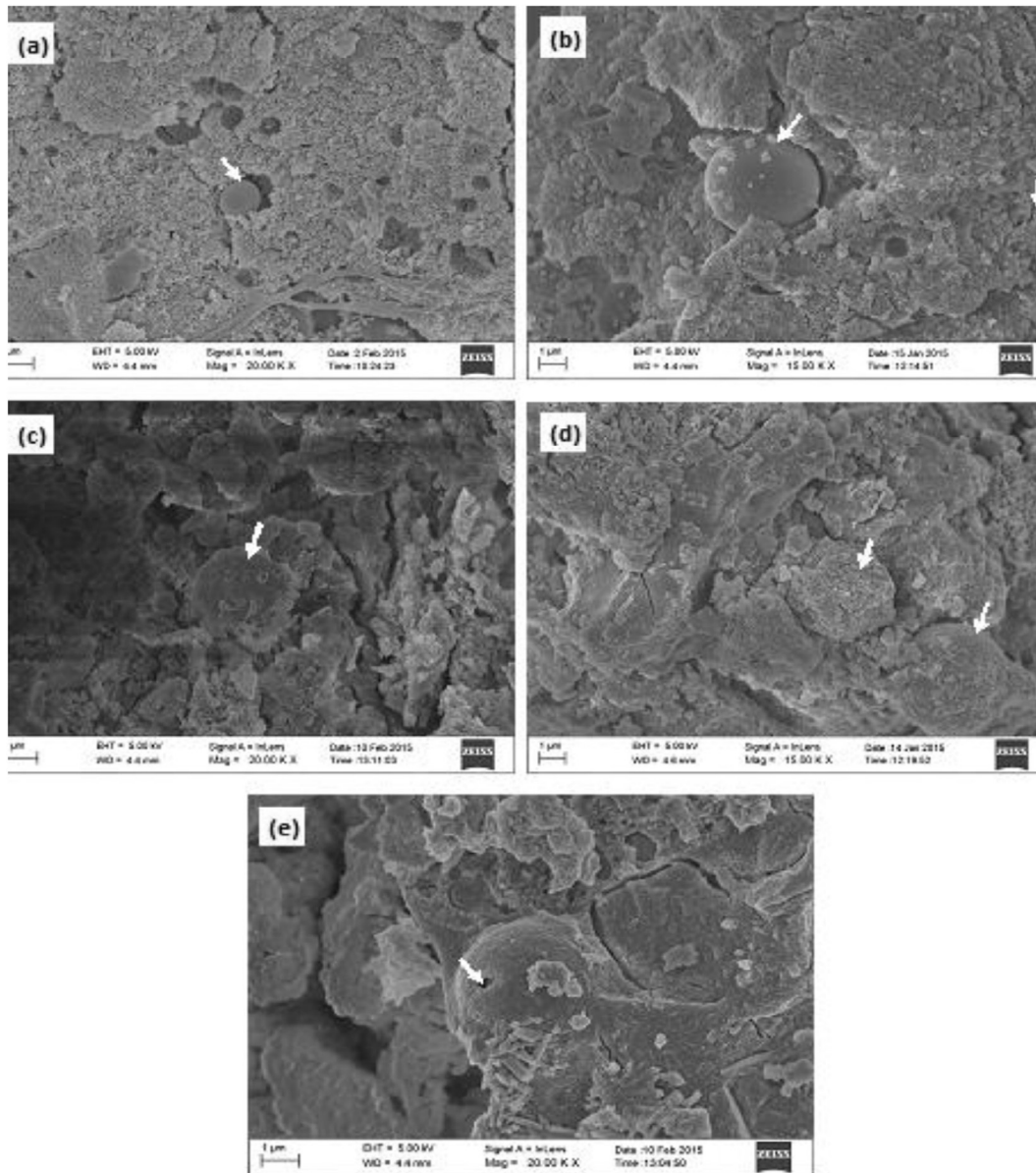


Fig. 3. Microstructure of fly ash-based geopolymer concrete with AAS-to-FA ratio of (a) 0.4 (b) 0.5 (c) 0.6 (d) 0.7 (e) 0.8 [11].

This phenomenon is explained when Rietveld refinement is carried out to analyse the crystalline phases in each sample. The following equation is used by Assaedi et al. [28] to determine the amorphous contents present in the sample [61].

$$W_{Am} = 1 - \sum_{i=1}^n W_n$$

where  $n$  is the number of crystalline phases refined.

As illustrated in Fig. 7, pure geopolymer (GP) has recorded the least amount of amorphous phases, which is in line with the amount of unreacted particles observed in Fig. 6(a). The addition of nano silica in the geopolymer nanocomposite mixes enhanced the amorphous content. Dry mix of nanocomposites believed to perform better due to the abilities to act as a filler in the geopolymer matrix. Thus, higher compressive strength is reflected, and fully reacted particles were observed in dry mix samples than wet mix samples.

Fig. 8 shows the interfacial transition zone (ITZ) between aggregate and geopolymer matrix. According to Embong et al. [21], the enhancement of the dissolution of fly ash particles and polycondensation of aluminosilicate compound provides bond between aggregates and matrix. As the formation of aluminosilicate filling the ITZ as shown, the compressive strength of the specimens was enhanced substantially. The presence of fiber straw in geopolymer matrix is suspected to be able to lower dissolution of fly ash particle. The unreacted fly ash particles were dispersed in the matrix as the water absorbent fiber straw covered the surface, as shown in Fig. 8(c).

Unlike Pavithra et al. [11], the microstructure of bottom ash and fly ash in geopolymer was studied by Xie and Ozbakkaloglu [19]. As the mass ratio of fly ash to bottom ash increases, the strength of the sample increases, too. The presence of bottom ash, however reduced the strength of geopolymer and it could be attributed to larger surface area of bottom ash with the presence of foreign objects that failed to react fully in the geopolymer (see Fig. 9).

The comparison between the Fig. 10(a) and (b) shows that a small amount of semi spheres was present along with some rectangular-shaped objects. While composition test revealed the presence of foreign object-radium, a radioactive earth-metal in the bottom ash, there were no foreign objects nor irregular-shaped particles found in fly ash. Other than the presence of foreign objects, some of the bottom ash did not react fully in the process of geopolymerization and this contributed to lower compressive strength compared to pure fly ash-based geopolymer.

Fig. 11 illustrated the microstructural analysis of FA-based geopolymer. Similar to previous studies, unreacted FA residues were observed as shown in the Fig. 11(a). Fig. 11(f) shows that only small traces sodium element observed on the non-reactive minerals covering the unreacted FA particles (2016). Fig. 11(b), (c) and (f), show the evidence of the production of geopolymer gels. Due to low calcium content present in Gaston FA, insignificant amount of calcium element can be seen in Fig. 11(d).

SEM image from Fig. 12 illustrated that crystalline phases were exposed, and new precipitant was formed after the dissolution of Gaston FA using alkaline solution. After the dissolution, parts A, B and C in Fig. 12 correspond to zeolite, mullite and hematite.

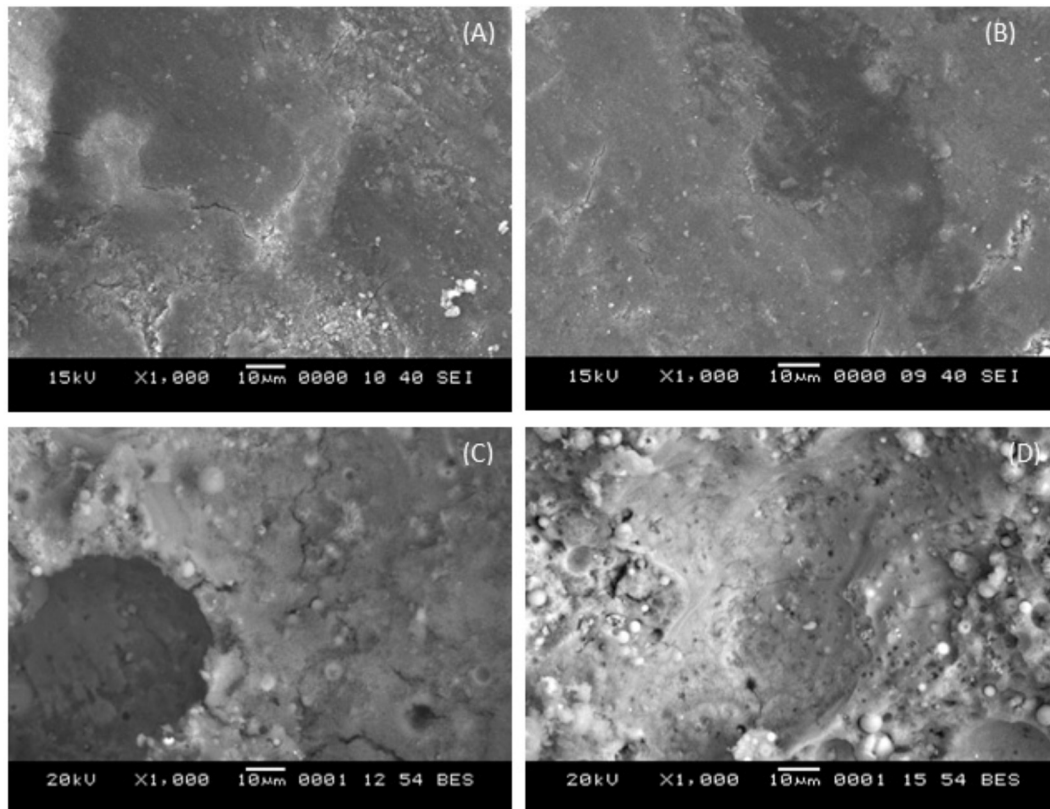


Fig. 4. Micrographs of fly ash-based geopolymers prepared at mass ratios of SS/SH at (A) 0.5, (B) 1.0, (C) 2.0, and (D) 3.0 for 28 days [49].

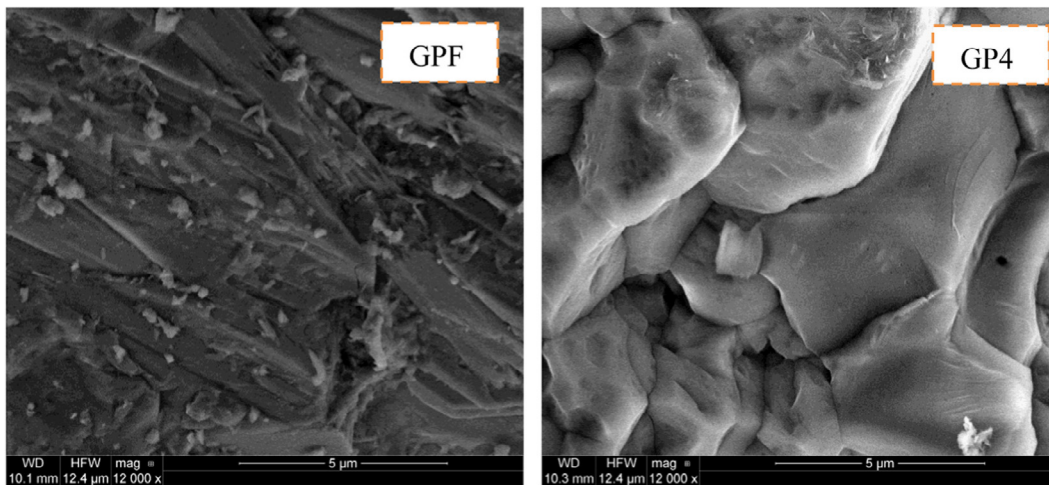


Fig. 5. SEM image of GPF and GP4 (28-day) [10].

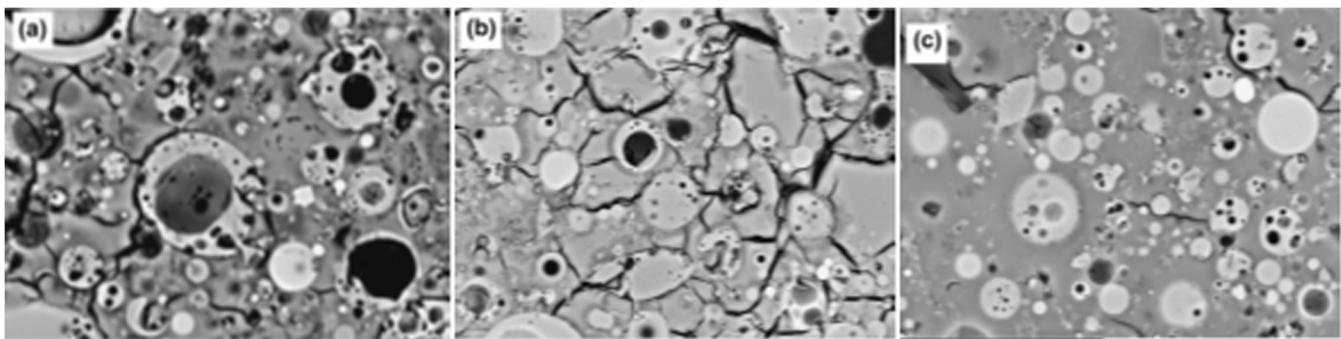


Fig. 6. Microstructure of (a) pure geopolymer with geopolymer nanocomposites containing 3.0% NS prepared by (b) wet-mixing, and (c) dry-mixing procedure [28].

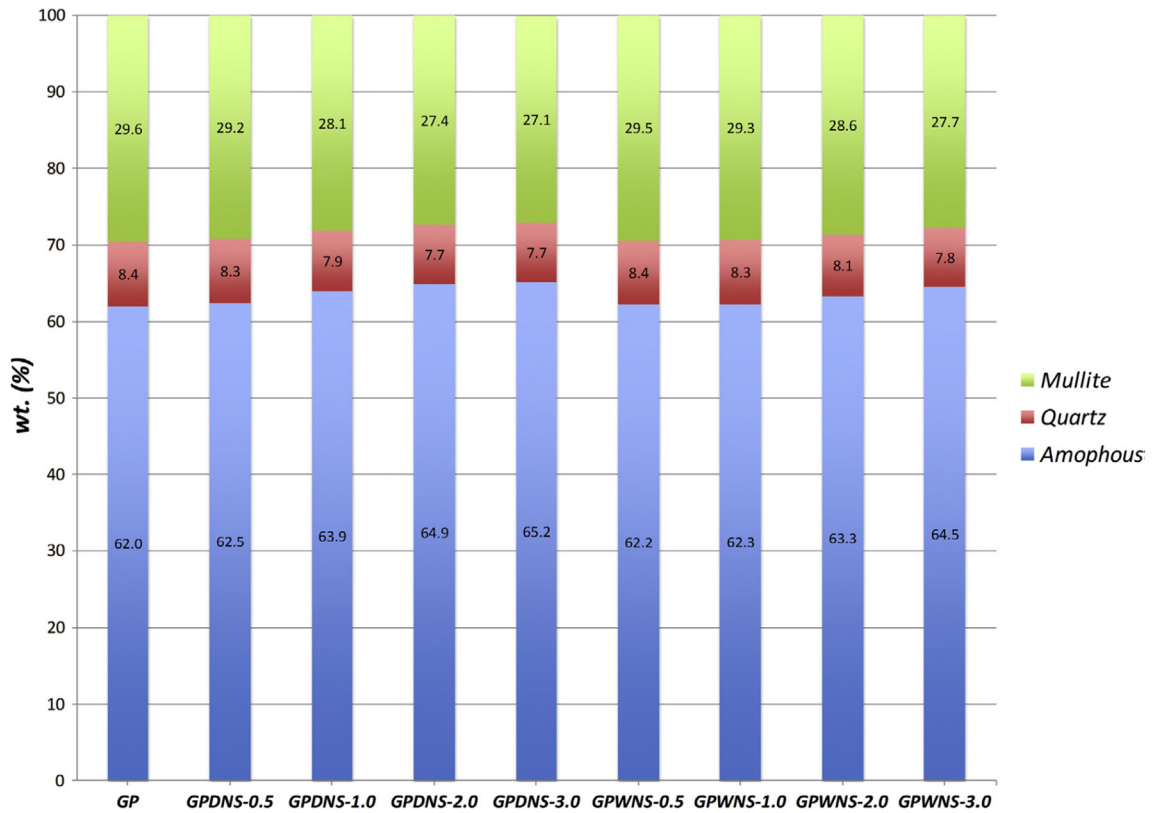


Fig. 7. Phases of amorphous and crystalline in pure geopolymer and geopolymer nanocomposites [28].

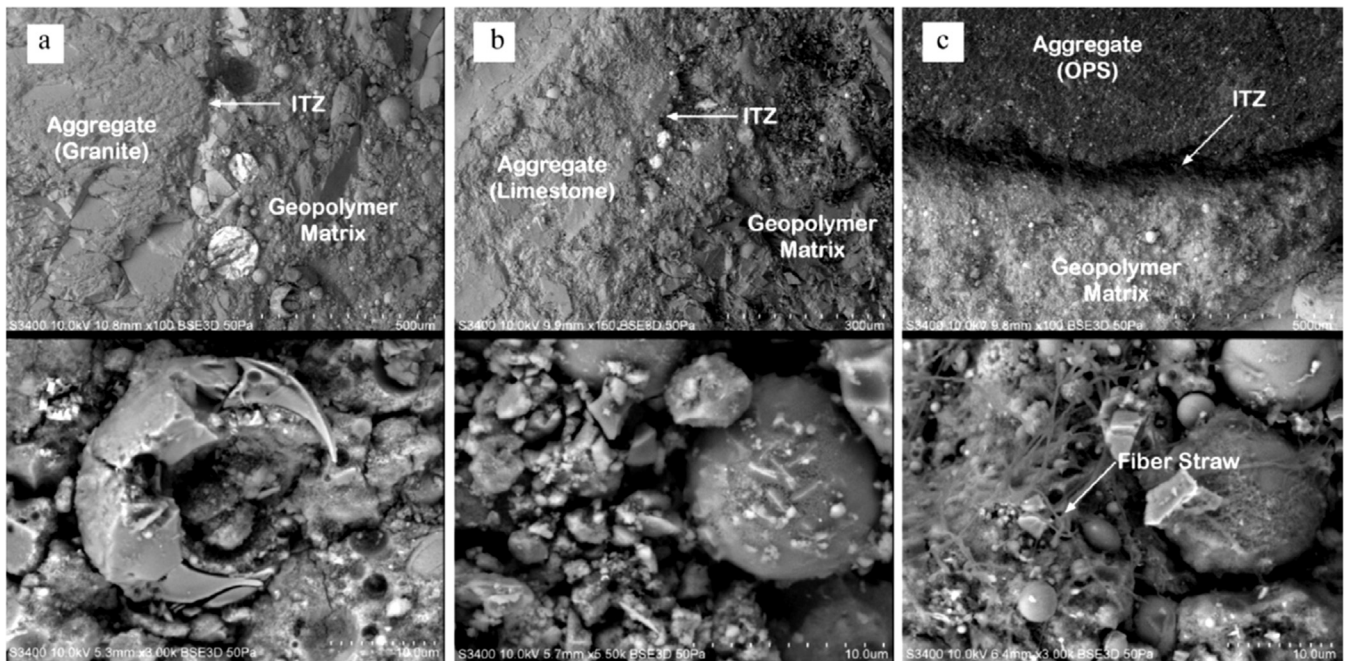
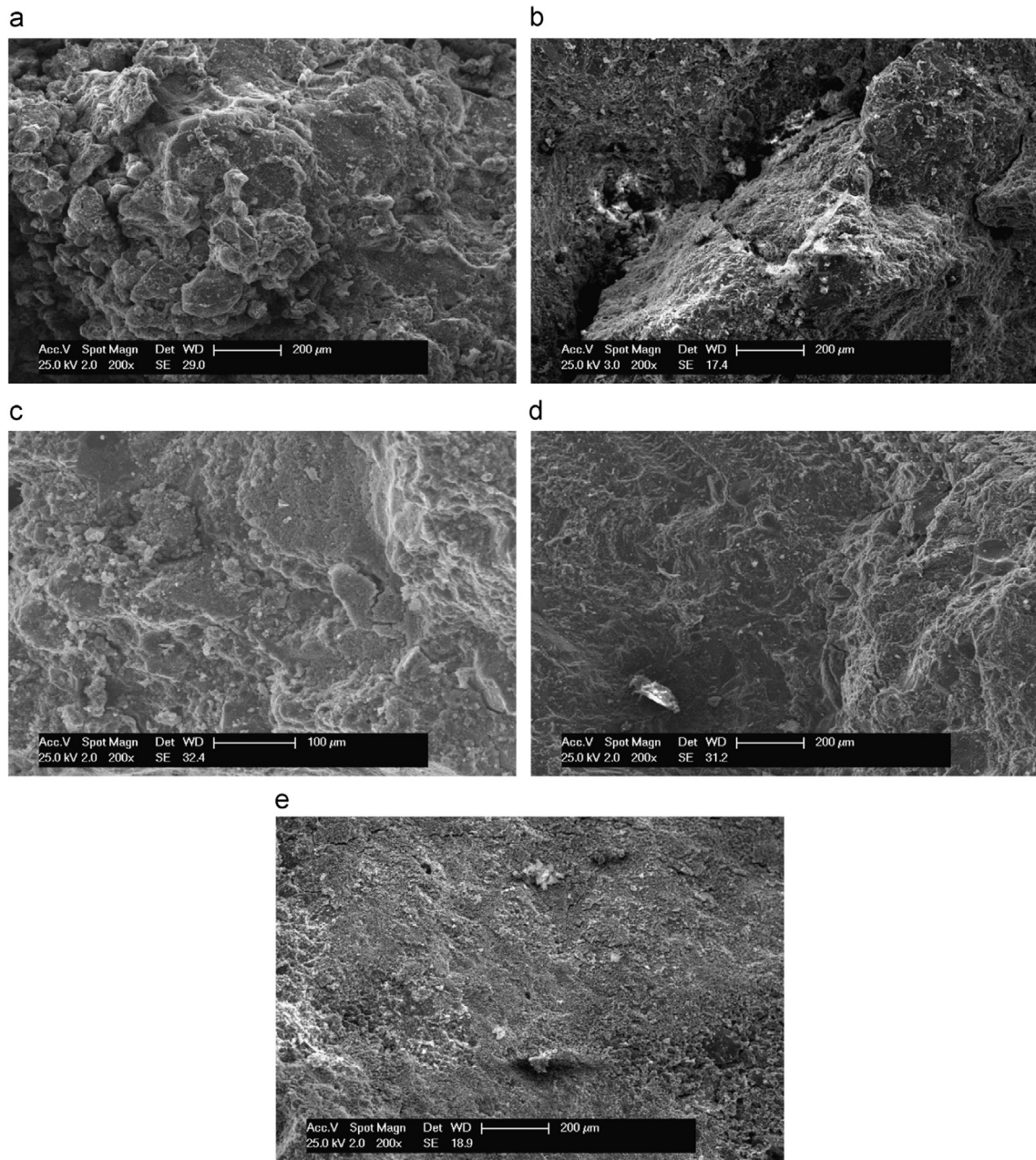


Fig. 8. SEM images of geopolymer concrete containing aggregates made up of (a) granite, (b) limestone, (c) oil palm shell [21].

**3.3.1.2. Palm oil fuel ash-based geopolymer.** A study was conducted by Kabir et al. [40] to learn the behavior of palm oil clinker (POC) and oil palm shell (OPS) as coarse aggregate with ternary binder of metakaolin (MK), ground granulated blast furnace slag (GGBS) and palm oil fuel ash (POFA)-based geopolymer concrete. POC aggregate is effective in enhancing the compressive strength due to the ability of binder to bond with the porous surface of POC [40]. A compact and denser matrix is illustrated in Fig. 13(a) while geopolymer concrete with microcracks were observed in Fig. 11(b). Unlike POC, OPS has smooth concave and convex surfaces.

**3.3.1.3. Metakaolin-based geopolymer.** The microstructure of metakaolin-based geopolymer in acidic-based (GPS4) and alkali-based (GPWP) was investigated by Tchakouté & Rüscher [37]. As illustrated in Fig. 14, morphology of the geopolymer cements was visualized at 120, 250 and 5000 magnifications. Large capillary pores and air bubbles were observed on the surface of the GPWP specimens whereas a number of microcracks was seen on the surface of GPS4. Throughout the process of dissolution and polycondensation, air bubbles trapped in the geopolymer cement paste attributed to large capillary pores. Lower compressive strength was recorded for the



**Fig. 9.** Microstructure shown at 200 $\times$  magnification: (a) B100 - 0.5 series; (b) B50 F50 - 0.5 series and (c) B25 F75 - 0.5 series; FA 100 - 0.5 A series and F100 - 0.25 series [19].

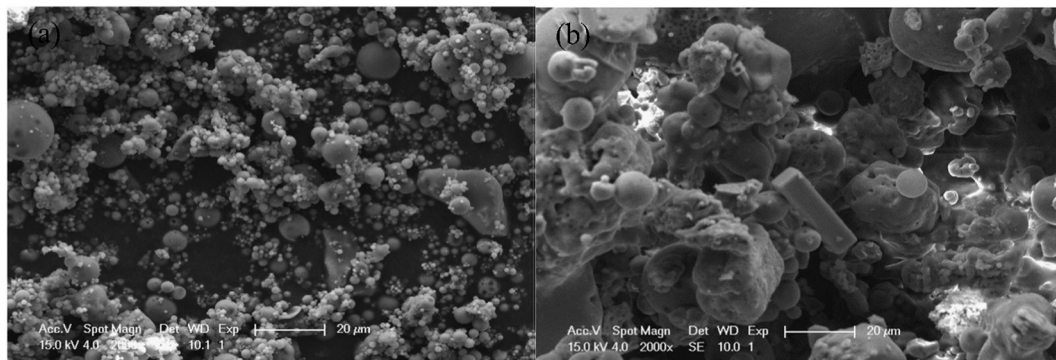


**Fig. 10.** Microstructure of the coal ashes at 2000 $\times$  magnification: (a) fly ash; and (b) bottom ash [19].

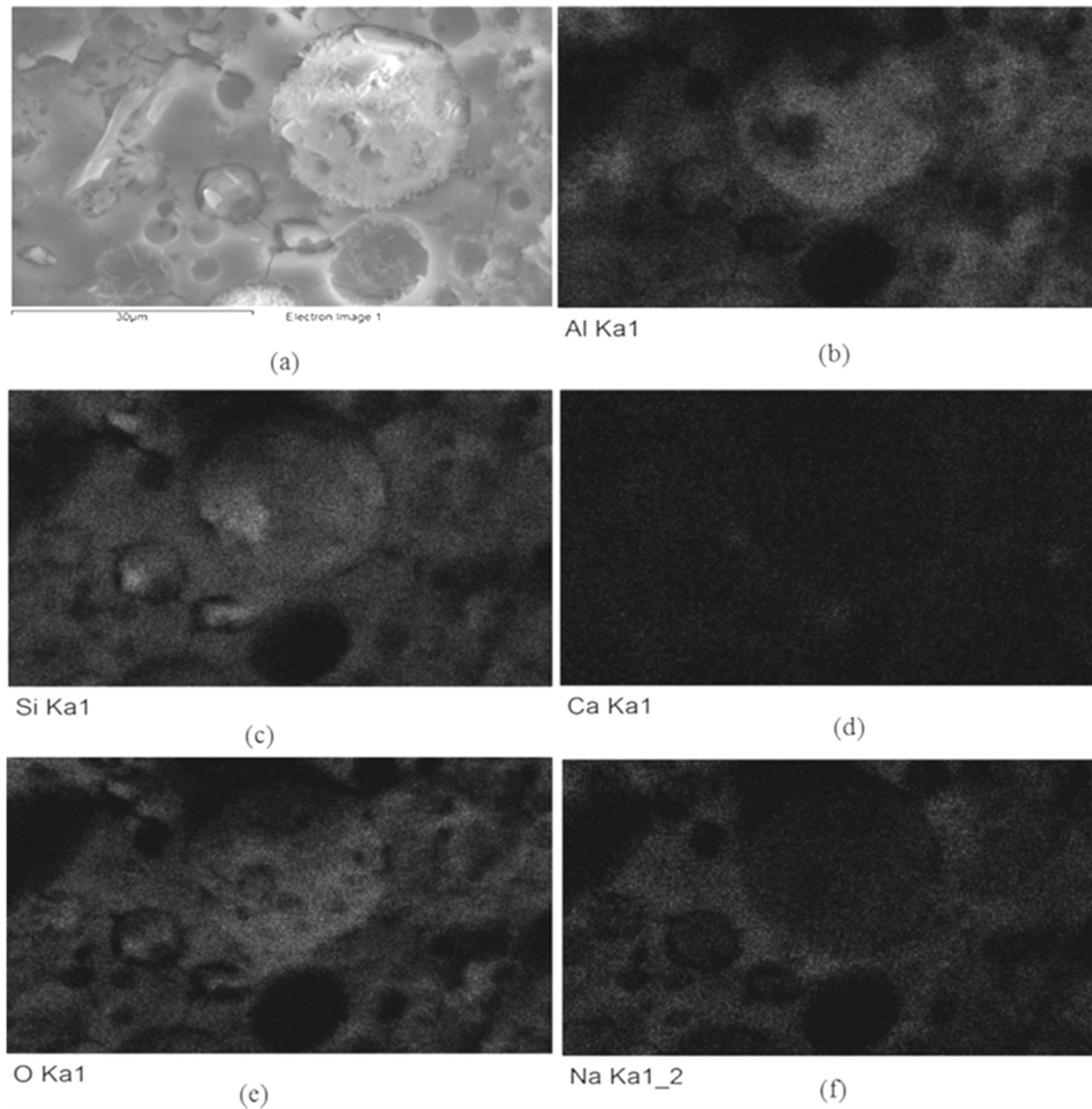


Fig. 11. Microstructure of (a) geopolymer made of Gaston fly ash, mapping of (b) aluminium, (c) silicon, (d) calcium, (e) oxygen and (f) sodium [32].

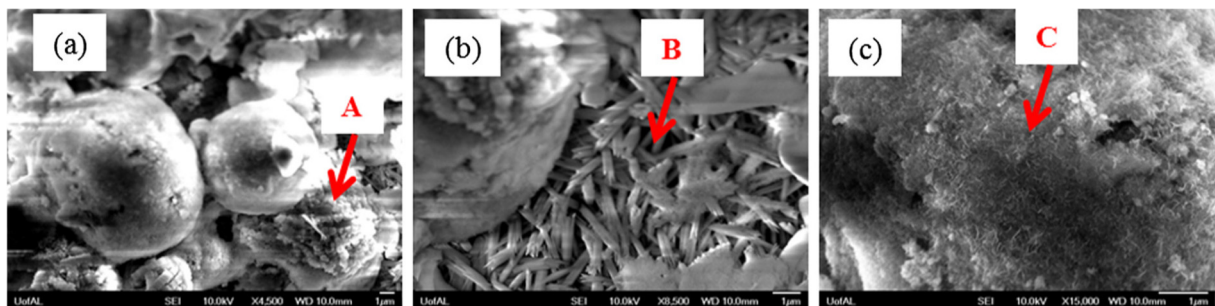


Fig. 12. Microstructure of Gaston fly ash after dissolution [32].

alkali-based geopolymer cements compared with the phosphate-based geopolymer cements due to the presence of large pores observed in GPWP specimens.

Micrograph analysis for 5000× magnification showed the presence of aluminium phosphate ( $\text{AlPO}_4$ ), later confirmed by XRD and FTIR tests. Aluminium phosphate, also known as berlinite is an isostructural mineral with quartz formed in the process of geopolymerization. Berlinite is known to react quickly even at ambient temperature due to its ability to dealuminate metakaolin in an acidic med-

ium. In addition, homogeneous and dense structures were observed for both geopolymer cements as a result of phosphoric acid and nano silica fume used as depolymerized hardeners.

As shown in Fig. 14, many cracks were detected in the micrographs analysis of GPS4 samples and those cracks were attributed to failure of specimens during compressive strength test. The high-density structure of phosphate-based geopolymer cement has block of poly (phosphor siloxo) chains where the forces applied from

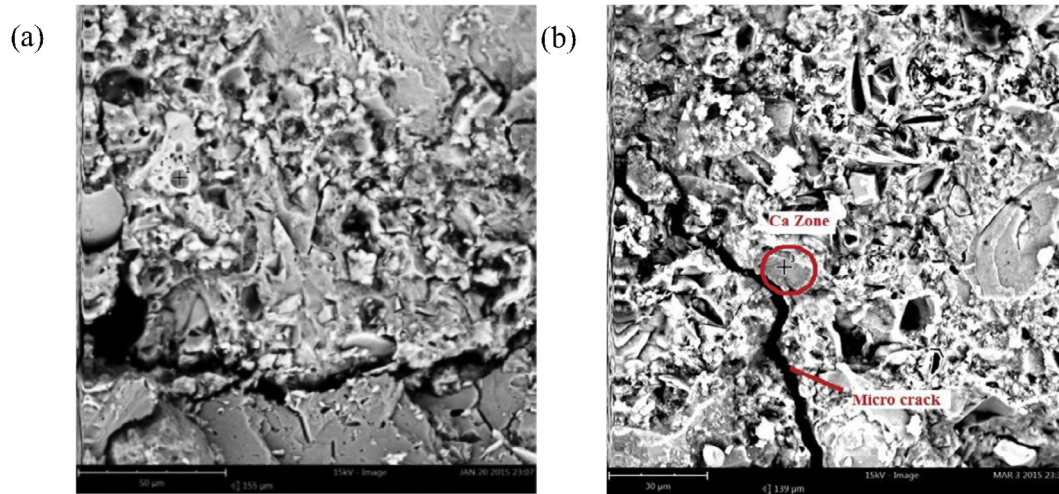


Fig. 13. Microstructure of MK-GGBS-POFA geopolymer concrete with (a) palm oil clinker (POC) and (b) oil palm shell (OPS) as aggregate [34].

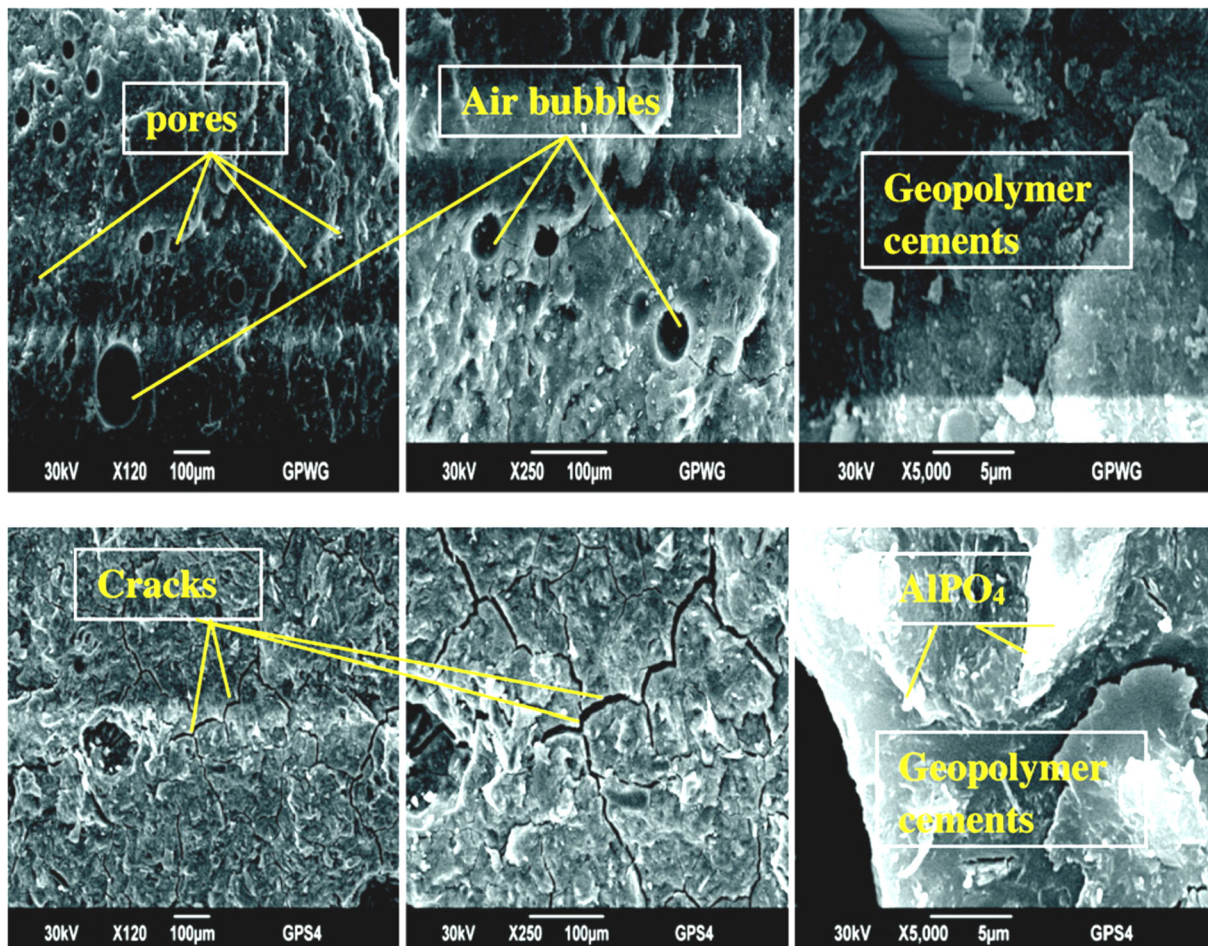


Fig. 14. Microstructure of metakaolin-based geopolymer cements in alkali medium (GPWG) and acid medium (GPS4) [37].

the machine was persisted. Effective bonding from both GPS4 and GPWP was noticed at higher magnification. Dense and compact matrixes hinted both alkali and acid-based geopolymer cements had good correlation in the process of geopolymerization.

**3.3.1.4. Ground granulated blast furnace slag-based geopolymer.** Sharmin et al. [44] has utilized high volume of GGBS along with metakaolin and rice husk ash (RHA). As illustrated in Fig. 15, a continuous compact microstructure is observed for the

optimum mix (0.25:0.25:0.50 for MK: RHA: GGBS). It is understood that mixes with high volume GGBS used to replace RHA, has subsequently improved the compressive strength. Utilize high volume of RHA is known for geopolymer with lower compressive strength and more brittle due to the larger solid particle and lower specific gravity of RHA [44,62].

Additional of MK in geopolymer was able to contribute stronger Si—O—Al and Al—O—Al bonds than the Si—O—Si bond. However, the utilization of high volume of MK is not advisable as it will produce sodium alumina silicate (zeolite) [63]. Zeolite is known for its negative effect on strength development as a result of excess

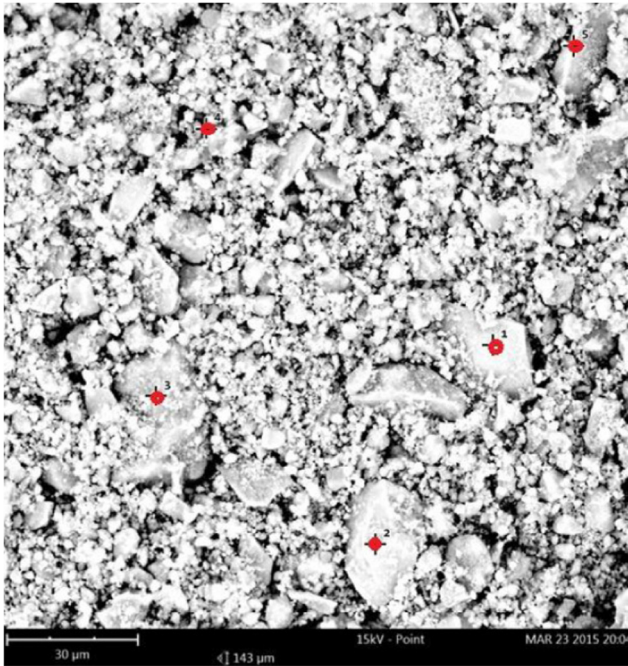


Fig. 15. Microstructure of RHA-MK-GGBS-based geopolymer mortar [44].

alumina from MK. Subsequently, the process of polymerization is hindered as high concentration of AAS was required to activate high volume of MK. Thus, the usage of MK in geopolymer needs appropriate consideration for achieving desired results.

Ye et al. [42] studied the early age and long-term microstructure of bauxite ore tailing and slag-based geopolymer paste. Fig. 16(a) demonstrated the microstructure of 28-days where porous gel with noticeable large pores were observed. It was predicted that continuous geopolymerization process has been able to produce the gels where large pores tend to reduce in small and volume for long-term specimen. Linking of geopolymer gels have formed capillary gels in pores and cracks which is illustrated in Fig. 16(b–d).

**3.3.1.5. Waste clay brick powder-based geopolymer.** Tuyan et al. [48] studied the microstructure of waste clay brick powder (WCBP)-based geopolymer and the SEM images are shown in Fig. 17. The unreacted WCBP particles (A) were observed with many voids (B) in the geopolymer matrix with 10%  $\text{Na}_2\text{O}$  and  $\text{SiO}_2/\text{Na}_2\text{O}$  ratio of zero as illustrated in Fig. 17(a). The comparison of Fig. 17(a) and (c) shows an increase in  $\text{SiO}_2/\text{Na}_2\text{O}$  ratio of 1.6.

resulted in more compact matrix and hence, higher compressive strength. On the other hand, denser structure was observed in Fig. 17(b) due to the higher  $\text{Na}_2\text{O}$  content in the geopolymer mixture; this enhanced the geopolymerization and as the result, the compressive strength was also increased. However, only slight improvement in the microstructure when the ratio of  $\text{SiO}_2/\text{Na}_2\text{O}$  was increased to 2.2 as shown in Fig. 17(d).

Fig. 17(e) and (f) present the effects of lower water-to-binder ratio in geopolymer which reduces the porosity of specimens. An increase in the curing period also enhanced the arrangement of the geopolymer structure effectively. As illustrated in Fig. 17(e), needle-like products (C) observed in the matrix hinted the presence of crystal phases of geopolymer matrix in the early age. As the curing period increase to 5 days, the compressive strength of the specimen increases while the needle-like products observed at Fig. 17(f) decreased significantly.

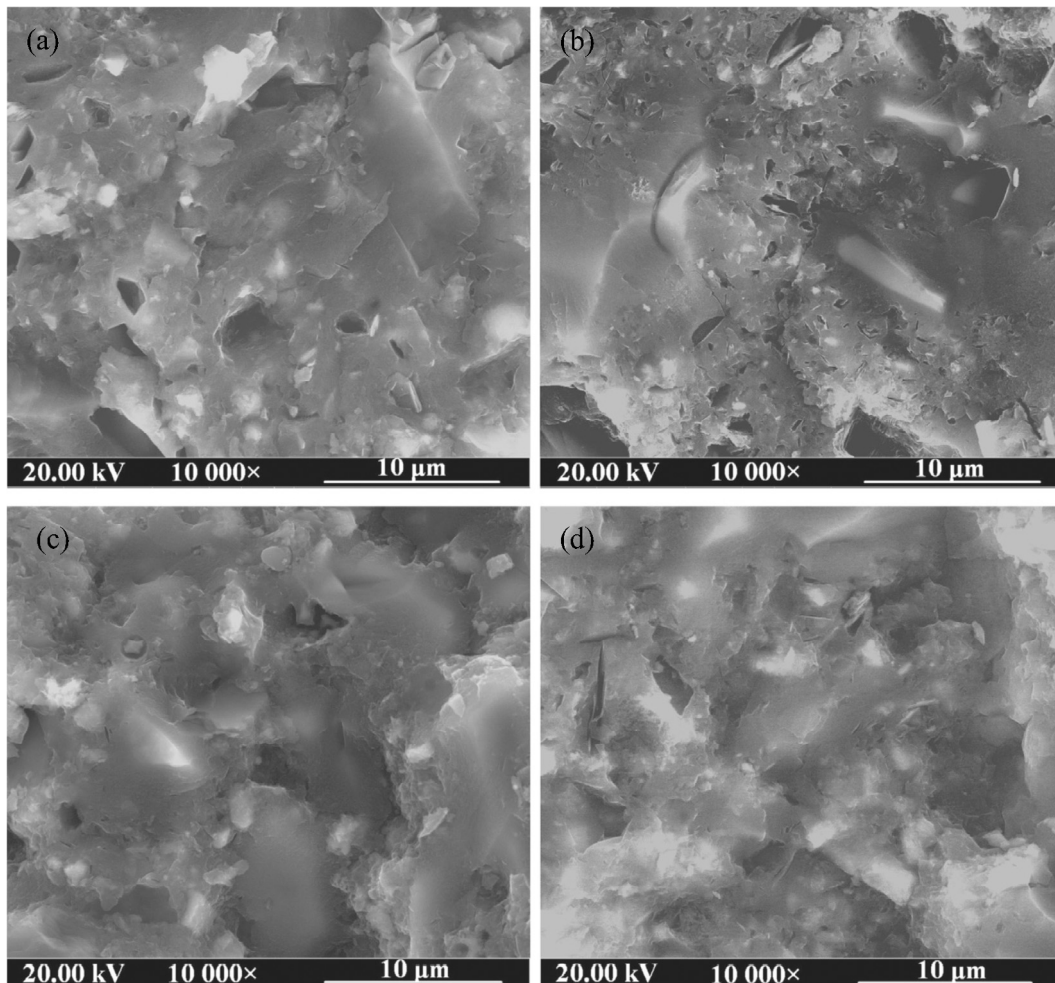
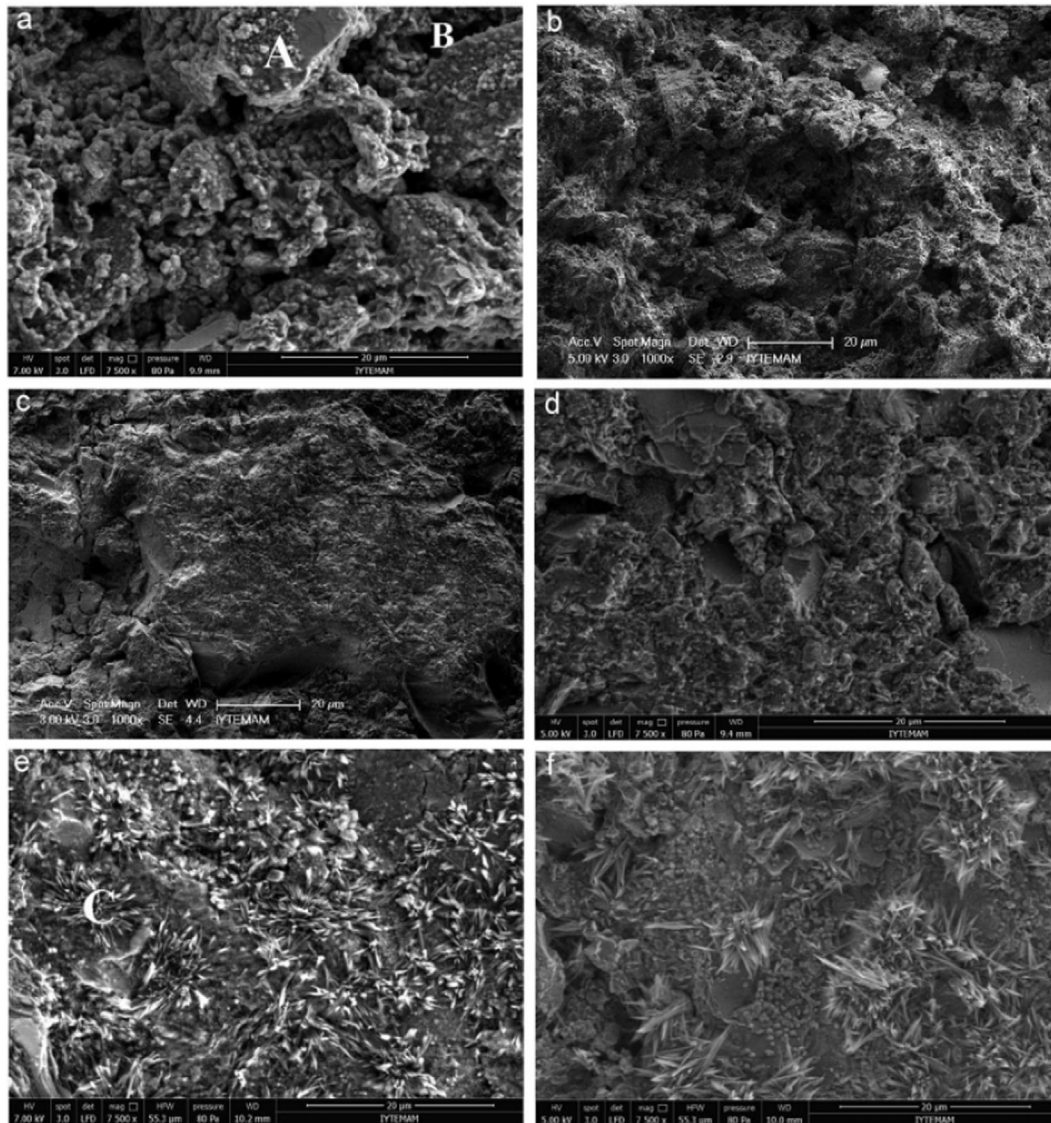
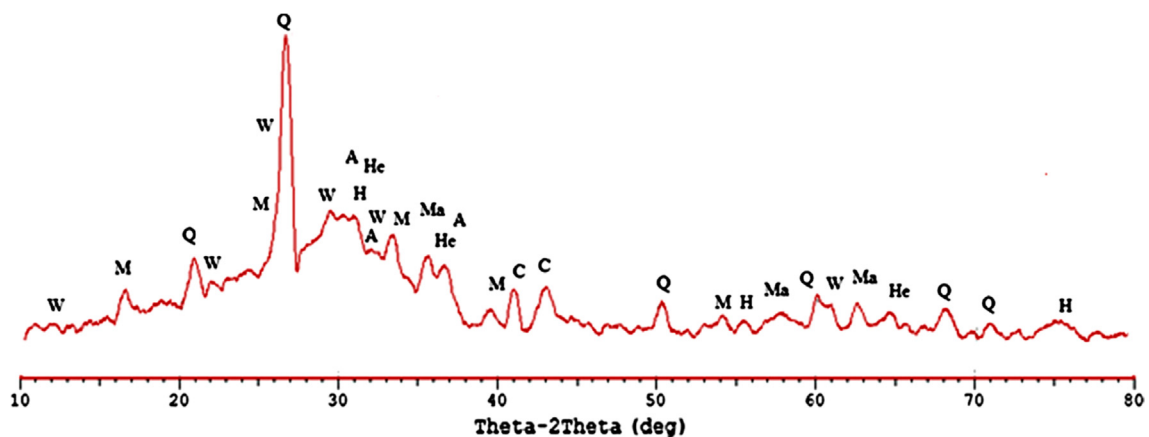


Fig. 16. Microstructure of (a) 28 days, (b) 2.5 years, (c) 4 years and (d) 6 years BOT and slag based geopolymer [42].



**Fig. 17.** Microstructure of waste clay brick powder-based geopolymers with (a) 10% Na<sub>2</sub>O, SiO<sub>2</sub>/Na<sub>2</sub>O: 0, (b) 4% Na<sub>2</sub>O, SiO<sub>2</sub>/Na<sub>2</sub>O: 1.6, (c) 10% Na<sub>2</sub>O, SiO<sub>2</sub>/Na<sub>2</sub>O: 1.6, (d) 10% Na<sub>2</sub>O, SiO<sub>2</sub>/Na<sub>2</sub>O: 2.2 (cured at 70 °C for 3 days), (e) 10% Na<sub>2</sub>O, SiO<sub>2</sub>/Na<sub>2</sub>O: 1.6 (80 °C for 24 h), and (f) 10% Na<sub>2</sub>O, SiO<sub>2</sub>/Na<sub>2</sub>O: 1.6 (80 °C for 5 days) [48].



**Fig. 18.** XRD analysis of unexposed FA geopolymer paste, where Q = quartz, M = mullite, Ma = magnetite, H = hematite, W = wollastonite, A = aegirine, C = calcium iron silicate, He = hercynite [28].

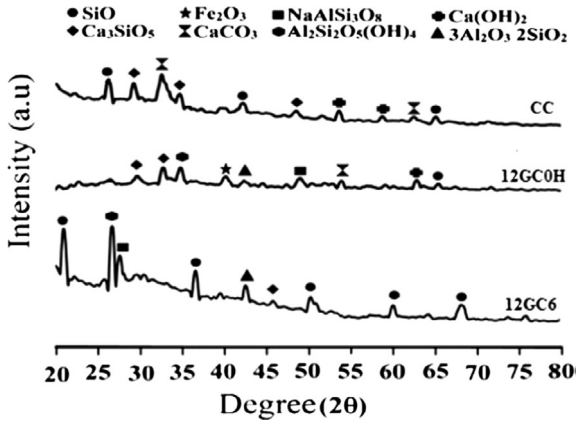


Fig. 19. XRD analysis of geopolymer concrete (12GC6 & 12GC0H) and control sample [22].

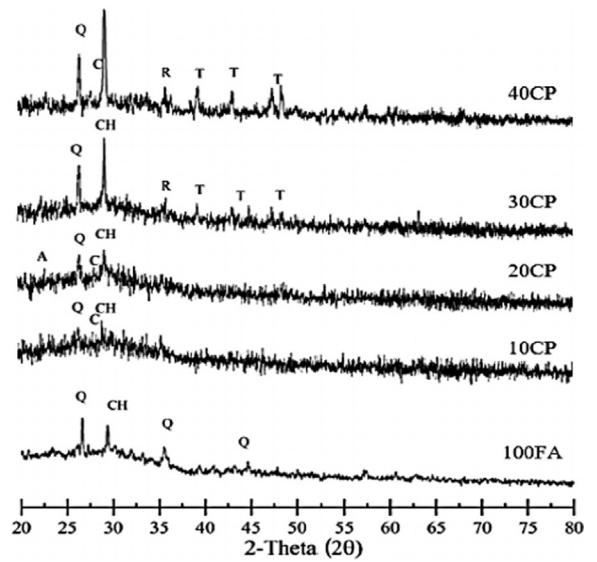


Fig. 21. XRD analysis of ground container glass powder and FA-based geopolymer paste where Q = Quartz, C = Calcite, CH = Calcium Silicate Hydrate, A = Calcium/Sodium Aluminate Silicate Hydrate, R = Cristobalite, T = Tridymite [33].

3.3.2. X-ray diffraction (XRD) of geopolymers

3.3.2.1. Fly ash-based geopolymer. Abdulkareem et al. [20], reported a broad hump from 20° to 35° indicating the present of amorphous geopolymer products. Based on previous studies, the presence of quartz and mullite reflected the composition

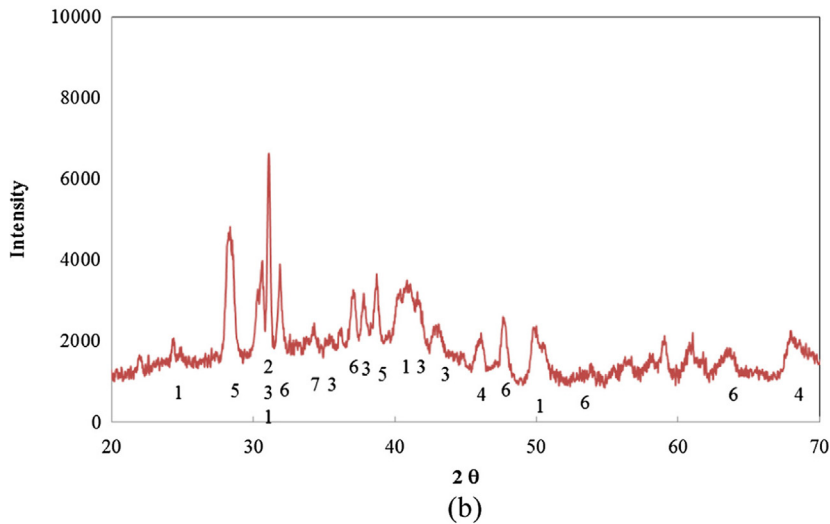
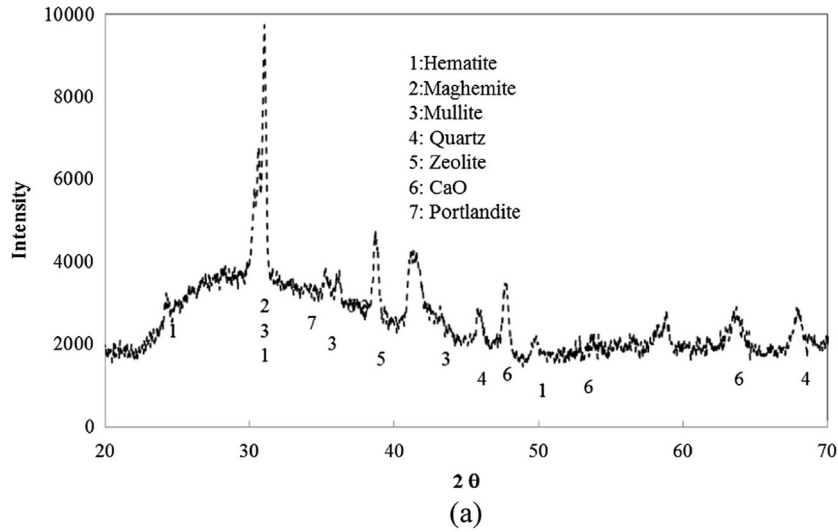


Fig. 20. XRD analysis (a) before and (b) after dissolution of fly ash [32].

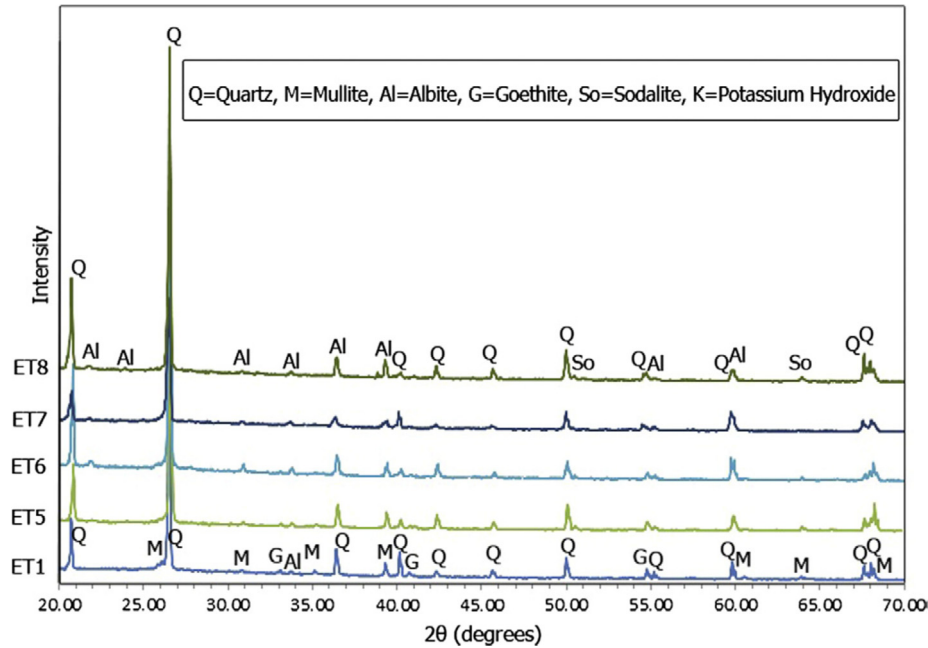


Fig. 22. XRD analysis for various composition of FA-POFA based geopolymer mortar [39].

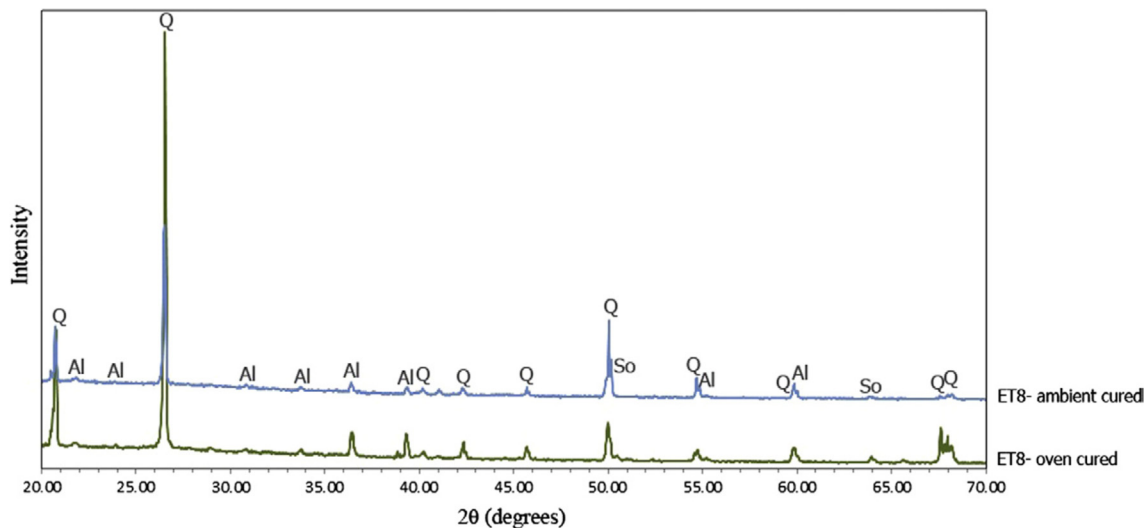


Fig. 23. XRD analysis for ambient and thermal cured POFA based geopolymer mortar [39].

of typical fly ash. As highlighted in Table 1, more than half of the fly ash was composed of iron and calcium. Thus, it explained the crystalline phases present in the geopolymer paste pattern as illustrated in Fig. 18.

The comparison of the cement-based control sample (CC) with geopolymer concrete- without the addition of nano silica (12GC0H) shows a wide hump around 25° to 35° in geopolymer concrete with nano silica (12GC6). The intensity of quartz, mullite and hematite was found higher in 12GC6 due to the presence of additional nano silica in the matrix as illustrated in Fig. 19. Some extra peaks are shown in nano silica modified geopolymer concrete (12GC6) which indicate the formation of the new phases of quartz ( $\text{SiO}_2$ ), albite ( $\text{NaAlSi}_3\text{O}_8$ ), kaolinite ( $\text{Al}_2\text{Si}_2\text{O}_5(\text{OH})_4$ ), alite ( $\text{Ca}_3\text{SiO}_5$ ), mullite ( $3\text{Al}_2\text{O}_3 \cdot 2\text{SiO}_2$ ) and  $\text{Ca}(\text{OH})_2$  crystalline compound compared to the others (12GC0H and CC concretes). The wide diffraction hump was detected around  $2\theta = 25^\circ\text{--}35^\circ$  which confirmed the presence of crystalline phases in 12GC6 geopolymer matrices.

As discussed earlier, crystalline phases were exposed after the addition of alkaline solution. The comparison of Fig. 20(a) and (b) shows reduction in the amorphous hump. The XRD analysis complements the SEM image as shown in Fig. 12. Zeolite was formed after the dissolution while mullite, quartz and hematite exist in all fly ashes.

Tho-In et al. [33] reported the XRD analysis at the age of 7-day of FA-based geopolymer paste with ground container glass (CP) as shown in Fig. 21. The FA-based geopolymer paste has a wide hump at 25° to 35° and low phases of calcite that corresponds to the high degree of geopolymerization [64]. The XRD trends of FA-CP pastes are similar to that of 100FA paste. However, peaks of quartz and calcite were observed as the percentage of ground CP increased due to the high contents of  $\text{SiO}_2$  and CaO [65]. Peaks of cristobalite and tridymite were noted at a higher percentage of CP replacement.

**3.3.2.2. Palm oil fuel ash-based geopolymer.** The XRD analysis for FA and POFA-based geopolymer mortars studied by Ranjbar et al. [24,39] is represented in Fig. 22. Similar to the previous studies, the FA and POFA-based geopolymer mortars were cured in oven at 65 °C for 24 h and then kept in room temperature for remaining 28-days. As evident from Fig. 22, a number of main crystalline phases of quartz, goethite, mullite and albite recorded. It is understood that phases of quartz, goethite and mullite were present due to FA while the presence of albite was further confirmed by FTIR analysis [39]. On the other hand, phases of quartz, albite and sodalite were recorded for the POFA-based geopolymer mortars. As the ratio of POFA used in the

FA-based geopolymer mortar increased, phase of albite which is also known as N-A-S-H, ( $\text{NaAlSi}_3\text{O}_8$ ) found to increase. It is shown that geopolymerization of POFA with alkali activators replaced the phases of mullite to albite due to insufficiency of Al specie in POFA. As illustrated in Fig. 22, the geopolymerization of POFA, FA and alkali activators led the amorphous to partial crystalline phases. Study was also conducted on heat cured and ambient cured FA and POFA-based geopolymer mortars. The comparison of Figs. 23 and 24 shows that both heat and ambient cured geopolymer samples had identical peak trend. Besides that, geopolymerization was not affected by the chemical contents of the FA and POFA-based geopolymer mortar samples cured at 65 °C and ambient temperature at different curing environments.

A different approach was studied by Tchakouté & Rüscher [37] as geopolymer cement prepared from acid and alkaline medium was analyzed and compared. The alkali-based and acid-based geopolymers were labelled as GPWP and GPS4 respectively, as shown in Fig. 25. A broad hump from 18° to 40° was recorded for both the acid and alkali-based geopolymer samples. As illustrated in the XRD patterns, the peak value recorded for both samples was around 27°. However, the XRD analysis for the MK as displayed in Fig. 26 recorded a broad hump range from 14° to 30° with the peak observed at 22°. The formation of the  $-\text{Si}-\text{O}-\text{P}-\text{O}-\text{Si}-$  and  $-\text{Si}-\text{O}-\text{Si}-\text{O}-\text{Al}-$  chain for both acidic and alkali-based geopolymer contributed to the deviation of the borad hump [37]. New phases of crystalline for the MK-phosphate-based geopolymer cement was observed in the XRD analysis.

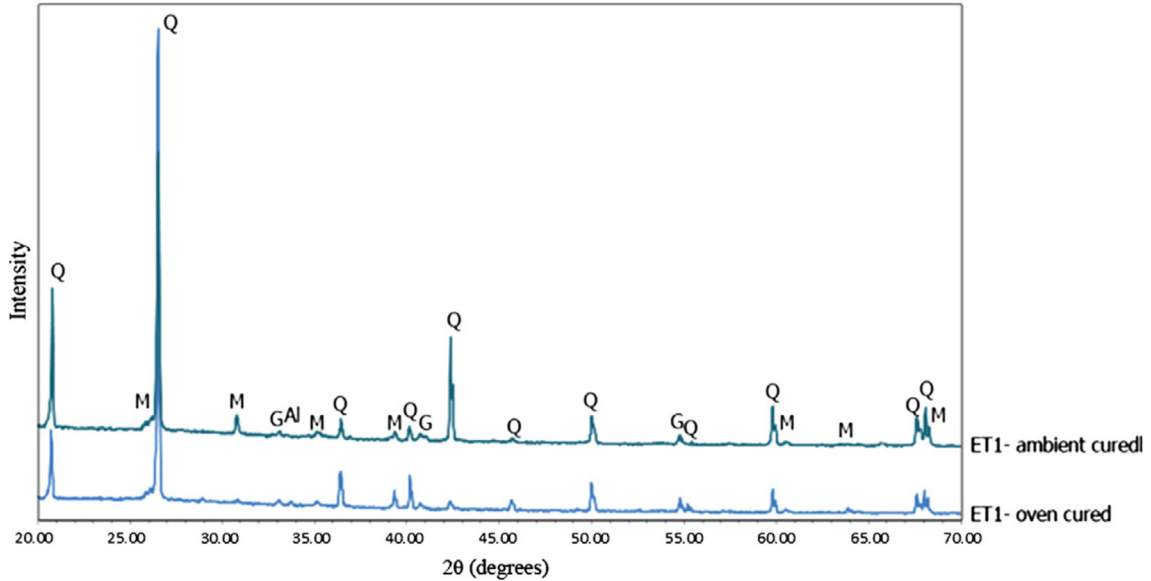


Fig. 24. XRD analysis for ambient and thermal cured FA based geopolymer mortar [39].

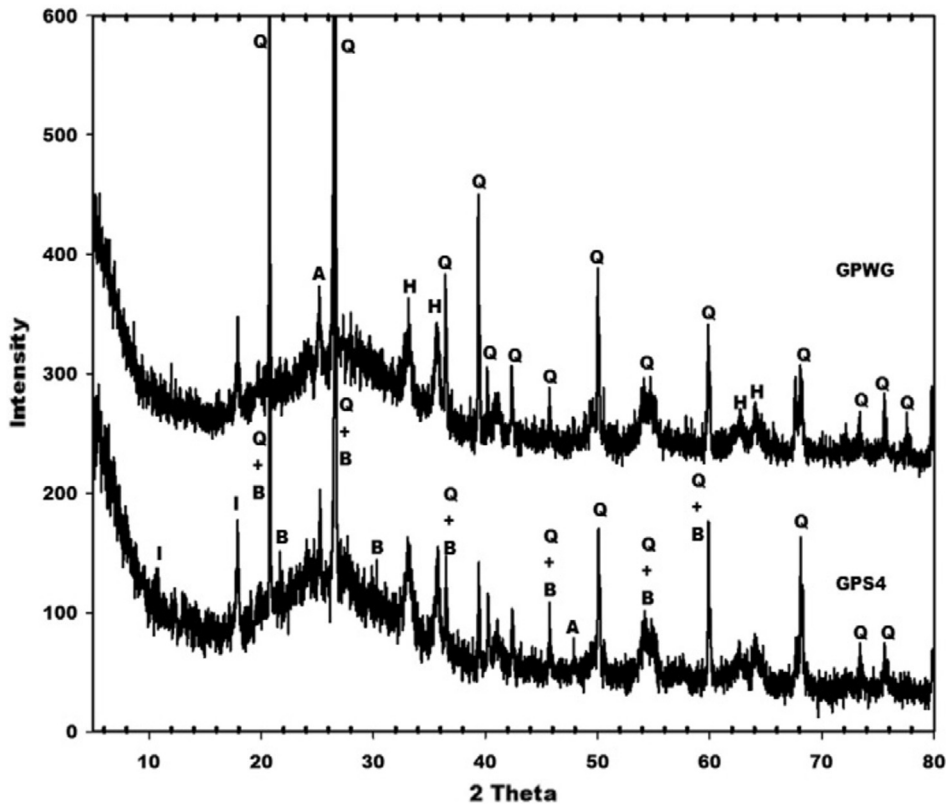


Fig. 25. XRD analysis for alkali (GPWP) and acid (GPS4)-based geopolymer cements, where H = hematite, A = anatase, B = berlinite, and Q = quartz [37].

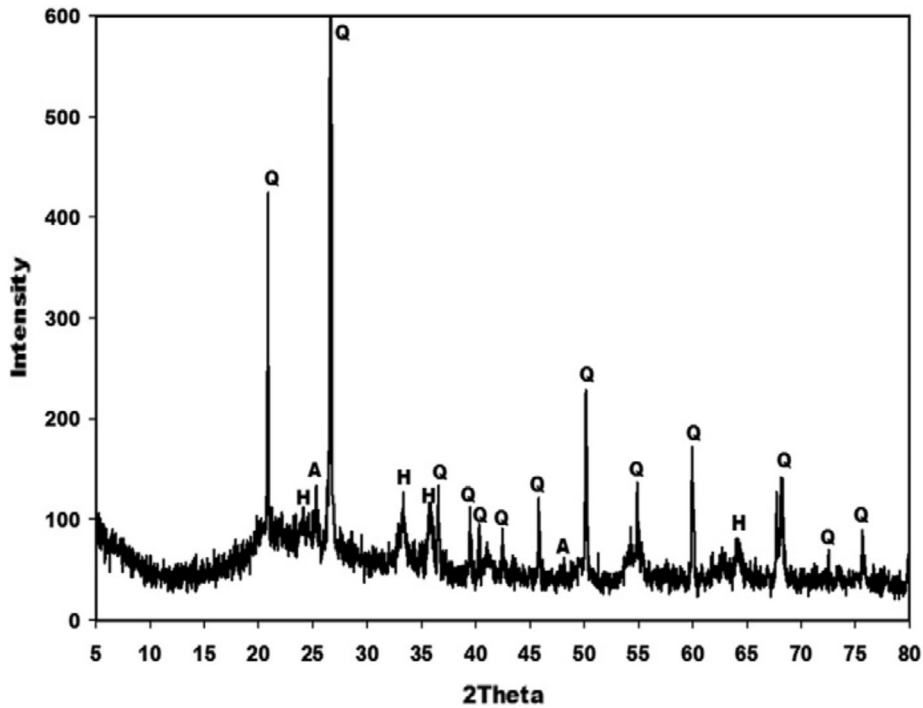


Fig. 26. XRD analysis for metakaolin (MK), where H = hematite, A = anatase, and Q = quartz [37].

The comparison of Figs. 25 and 26 shows that a number of peaks from MK confirmed with the geopolymer sample. Both acidic and alkali-based geopolymers, as well as MK recorded the phases of anatase, hematite and quartz. Withstanding with previous studies, the aforementioned minerals remain unchanged even after the process of geopolymerization.

3.3.2.3. *Metakaolin-based geopolymer.* The characteristic of metakaolin (MK) in hardened geopolymer paste at initial state (GP), thermally exposed geopolymer paste (EGP) and ceramic grog (CG) was studied using XRD analysis. MK's major compositions are monoclinic illite, hexagonal quartz, anorthic kaolinite and orthorhombic mullite as shown in Fig. 27 [45]. A small amount of tetragonal

anatase and rutile were also found alongside. A broad hump was also detected in the XRD pattern of MK. On the other hand, a broad diffuse peak was observed in the GP sample. The peak ranges from 20° to 31° is closely related with the amorphous aluminosilicates where the primary phase of the geopolymer was formed [66]. However, a comparison of MK and GP revealed that exceptionally high amount of kaolinite and illite phases was reduced after the process of geopolymerization. Unlike illite and kaolinite, quartz and mullite phases were found to remain inactive.

Slight changes from the phase composition were observed after the geopolymer was treated at 1000 °C. Kaolinite phase has decomposed completely as displayed in Fig. 27. The amount quartz decreased considerably while hardly any changes in the

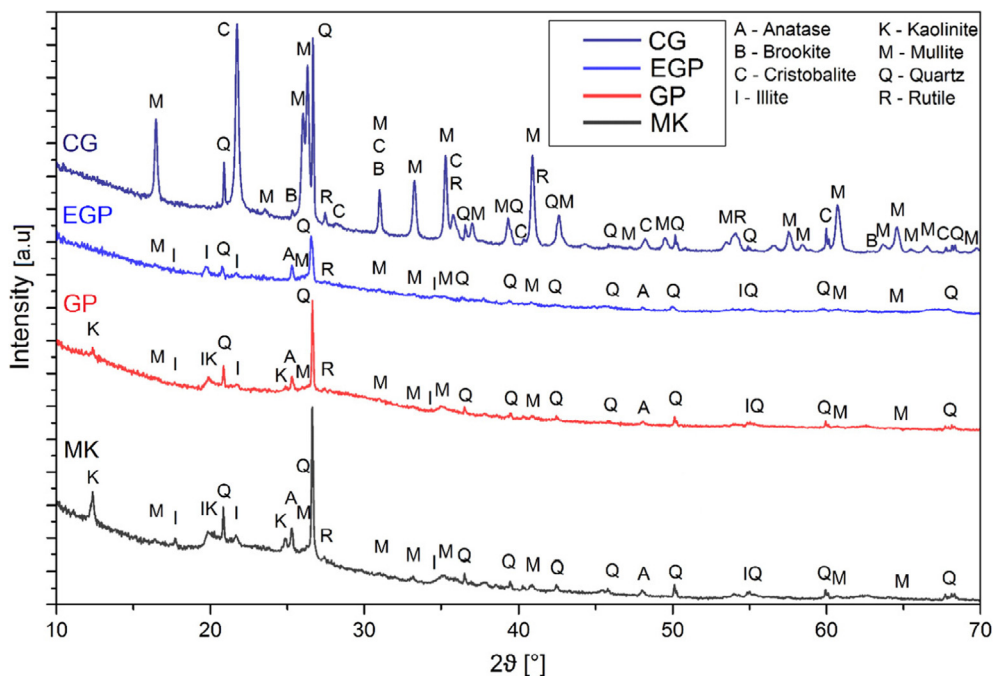


Fig. 27. XRD analysis of metakaolin (MK), hardened geopolymer paste in initial state (GP), exposed geopolymer paste (EGP) and ceramic grog (CG) [45].

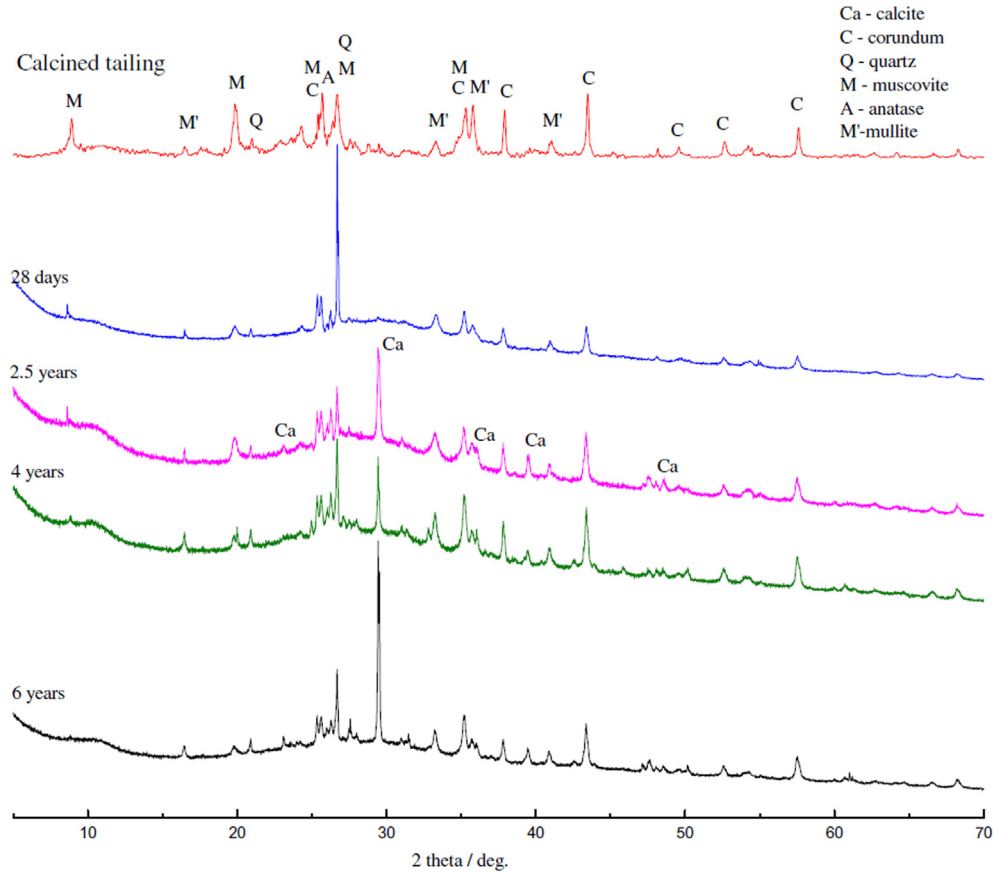


Fig. 28. XRD analysis of early age to long term geopolymer paste and bauxite ore tailing [42].

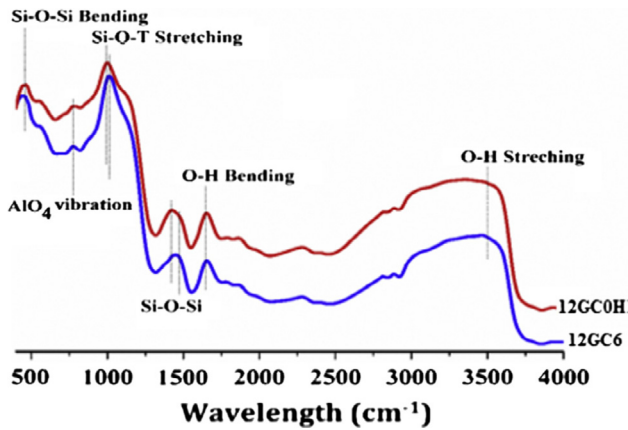


Fig. 29. FTIR analysis of geopolymer concrete (12GC6 & 12GC0H) [22].

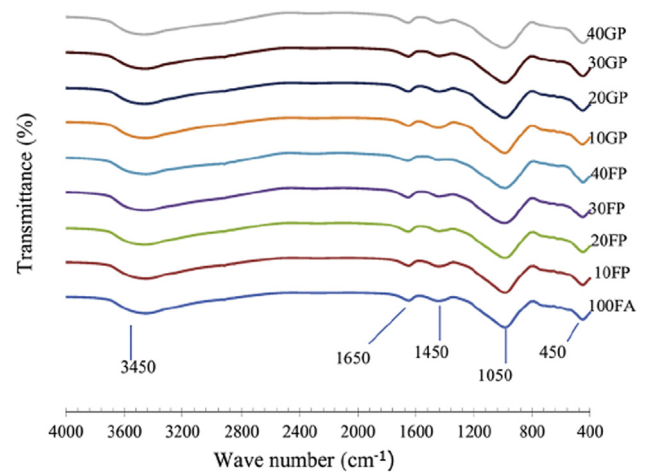


Fig. 30. FTIR analysis of FA-based geopolymer with ground fluorescent lamp (FP) and container glass (GP) [33].

contents of illite, mullite, anatase and rutile were recorded. Inconsistent with the findings from He et al. [57], the results obtained by Kovářík et al. [45] demonstrated that no detectable amount of kalsilite or leucite crystalline phase during the thermal treatment at 1000 °C. It was predicted that the different chemical contents from the samples used was the main cause for the contradiction in the findings.

3.3.2.4. *Ground granulated blast furnace slag-based geopolymer.* Fig. 28 represented the development of phases of geopolymer from early age to long-term specimen. The high intensity peak, 2θ for 28 days geopolymer paste is reported at 27°. A number of minerals from bauxite ore tailing such as corundum, muscovite, anatase, quartz and mullite are still identified for long-term specimen. However, formation of calcite mineral is detected in the long-term specimens which hinted the specimen is susceptible to carbonation.

3.3.3. *Fourier transform infrared spectroscopy (FTIR)*

3.3.3.1. *Fly ash-based geopolymer.* A FTIR analysis was carried out by Adak et al. [22] to determine the structure of geopolymer. The infra-red spectroscopic results of 12GC6 and 12GC0H samples are shown in Fig. 29. The distinct intensity band near 460 cm<sup>-1</sup> was recognized for the Si—O—Si bending vibration. The band between 750 cm<sup>-1</sup> and 800 cm<sup>-1</sup> was observed due to the AlO<sub>4</sub> vibration. Another peak for the asymmetric stretching and vibration band of Si—O—T (T = Al, Si) which was described as the strongest band, registered in the region of 950 cm<sup>-1</sup>–1050 cm<sup>-1</sup> [67]. The position (1420 cm<sup>-1</sup>) of Si—O—Si in 12GC0H was shifted to the right position (1485 cm<sup>-1</sup>) in 12GC6. A significant band was also located at approximately 3450 cm<sup>-1</sup> for OH stretching bonding.

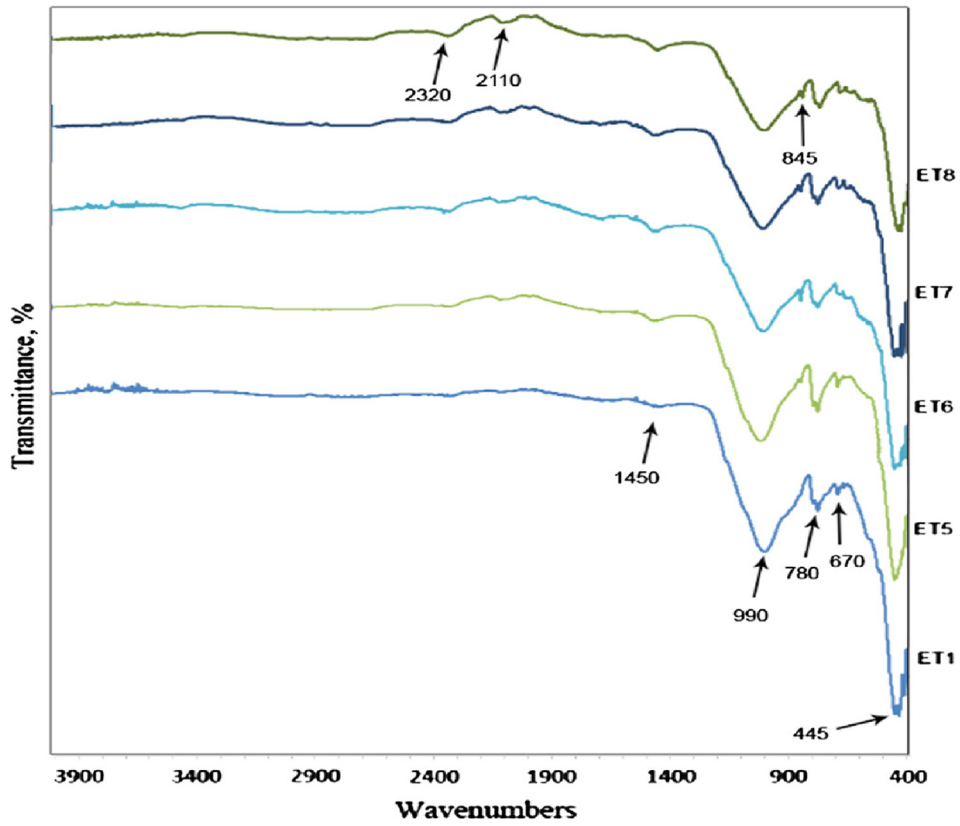


Fig. 31. Fourier transform infrared spectra of POFA-FA base geopolymer [39].

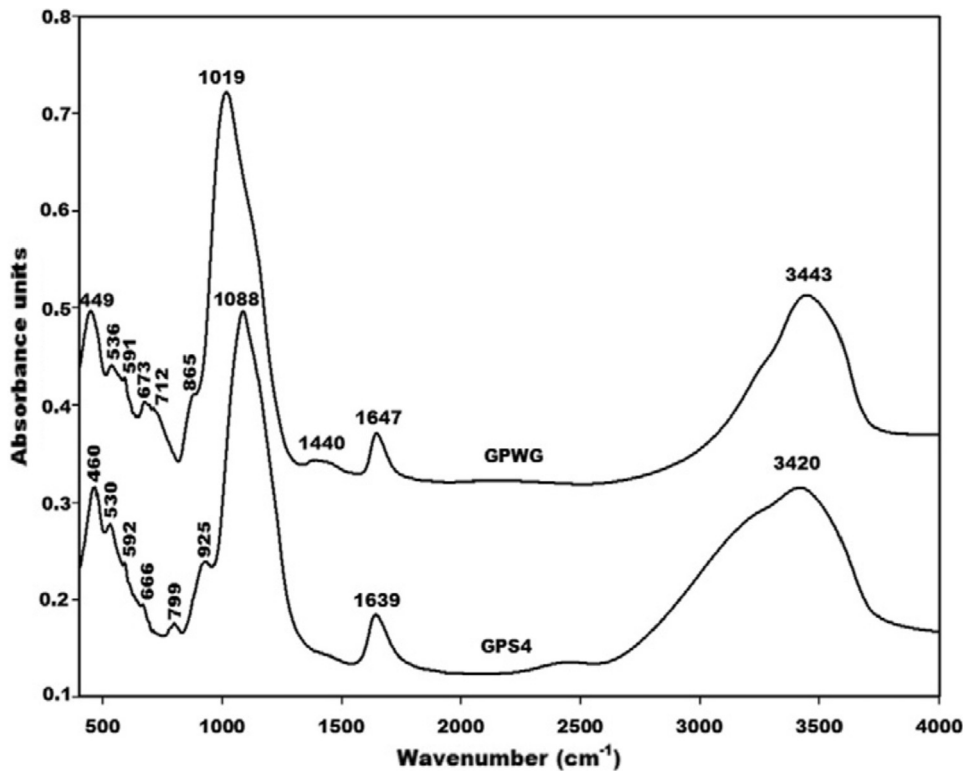


Fig. 32. KBr-IR spectra of alkali (GPWP) and acid (GPS4)-based geopolymer cements [37].

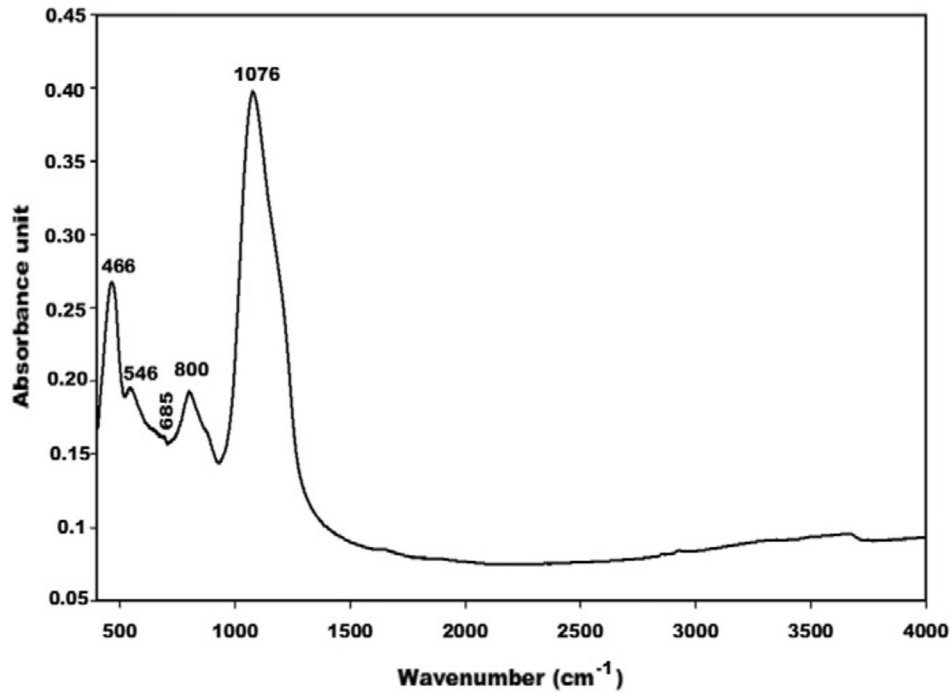


Fig. 33. IR spectrum of metakaolin (MK) [37].

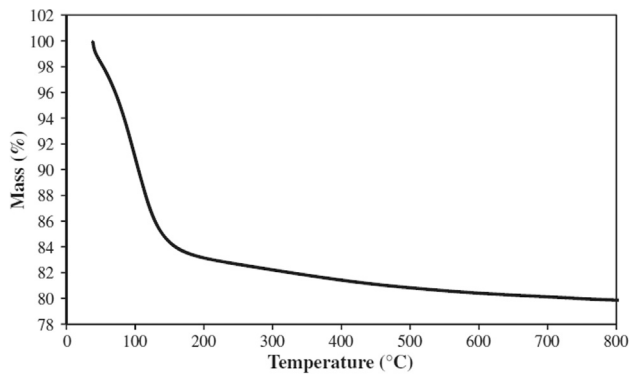


Fig. 34. TGA curve of the fly ash-based geopolymer paste [20].

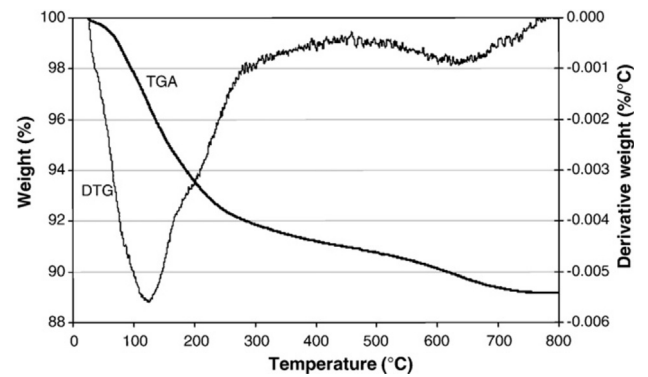


Fig. 36. TGA and DTG of fly ash geopolymer paste [18].

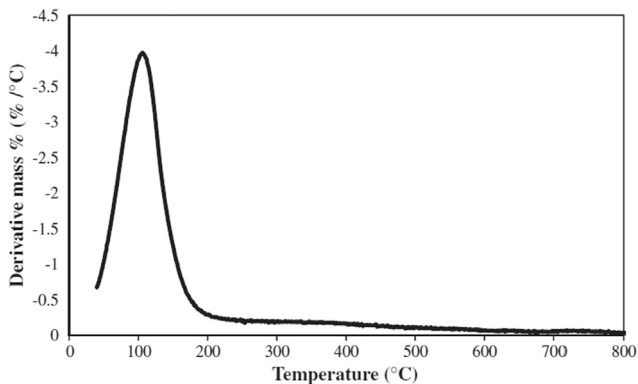


Fig. 35. DTG curve of the fly ash-based geopolymer [20].

Tho-In et al. [33] conducted the FTIR analysis on FA-based geopolymer with ground fluorescent lamp (FP) and container glass pastes. As displayed in Fig. 30, the absorption bands at approximately  $3450\text{ cm}^{-1}$  and the weak band

at  $1650\text{ cm}^{-1}$  are associated with the vibrations of O–H and H–O–H bonds in the water molecules. Previous studies reported that the bands as reported by Tho-In et al. [33] revealed that the water molecules were absorbed on the surface or embedded in the pores during the process of geopolymerization [68,69]. The band at roughly  $1450\text{ cm}^{-1}$  indicated the extension of O–C–O in carbonate groups due to reaction of alkali metal hydroxides with atmospheric  $\text{CO}_2$  [70,71]. The irregular stretching of Si–O–X bonds found in all specimens is located at  $1050\text{ cm}^{-1}$ , where X representing a tetrahedral silicon or aluminium atom. The Si–O–X bond supported the geopolymerization process with the phases of amorphous aluminosilicates formed. Besides, researchers also stated that the sharp absorption band correlates to the number of tetrahedrally coordinated aluminium that exist in the geopolymer gel [72,73]. Furthermore, the stretching of O–Si–O and Si–O–Si bonds which can be located at  $450\text{ cm}^{-1}$  is identical to those Si–O–Al group [74].

In addition, the matching broad bands were reported for both 100 FA and FA with GP and FP specimen as shown in Fig. 30. On the other hand, specimen of 100 FA recorded the higher rate of geopolymerization due to the absorption band at  $1050\text{ cm}^{-1}$  was higher than that of GP and FP specimens.

**3.3.3.2. Palm oil fuel ash-based geopolymer.** Ranjbar et al. [24,39] also studied the differences of geopolymer specimen with FTIR analysis. As reported in Fig. 31, pure POFA-based geopolymer sample (ET8) has major band of 2300, 2110, 1450, 990, 845, 670 and  $445\text{ cm}^{-1}$  while 1450, 990, 670 and  $445\text{ cm}^{-1}$  for FA-based geopolymer

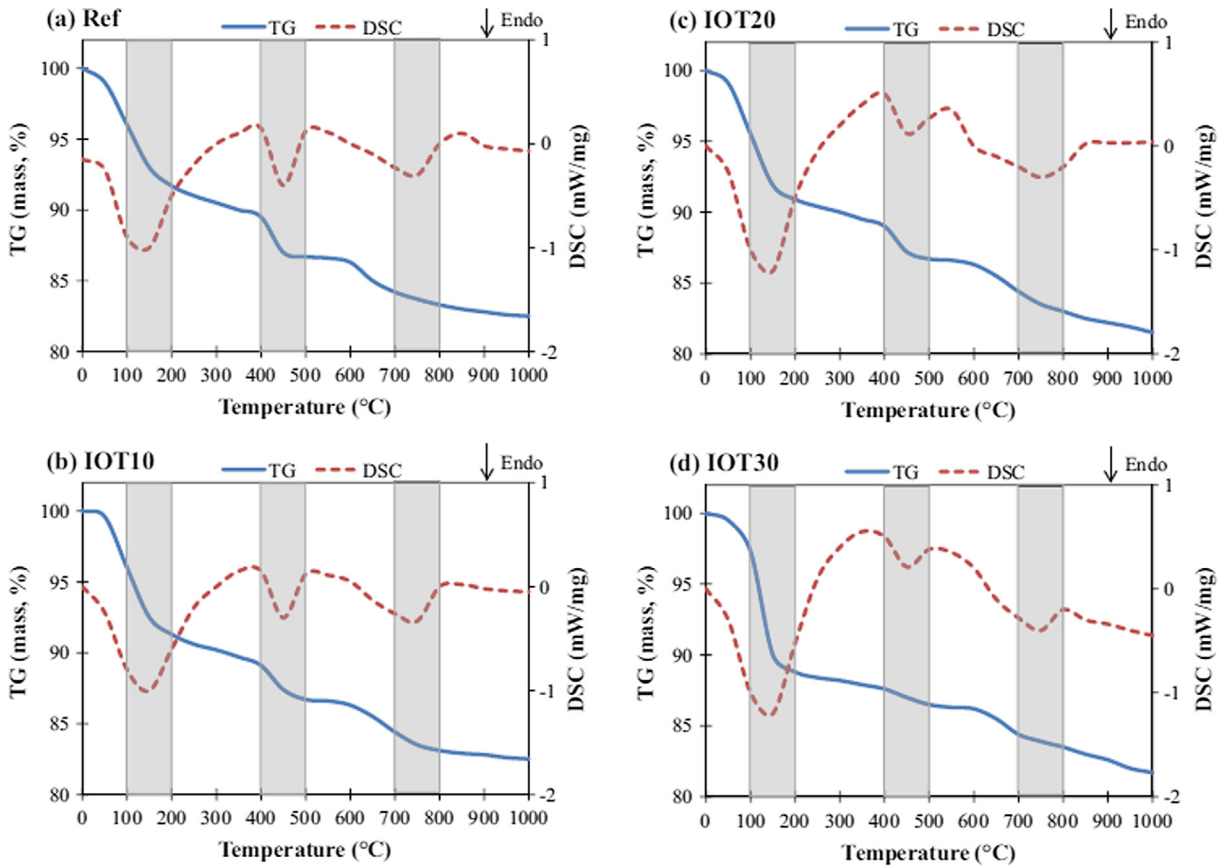


Fig. 37. Thermal analysis for geopolymer pastes incorporating IOT [8].

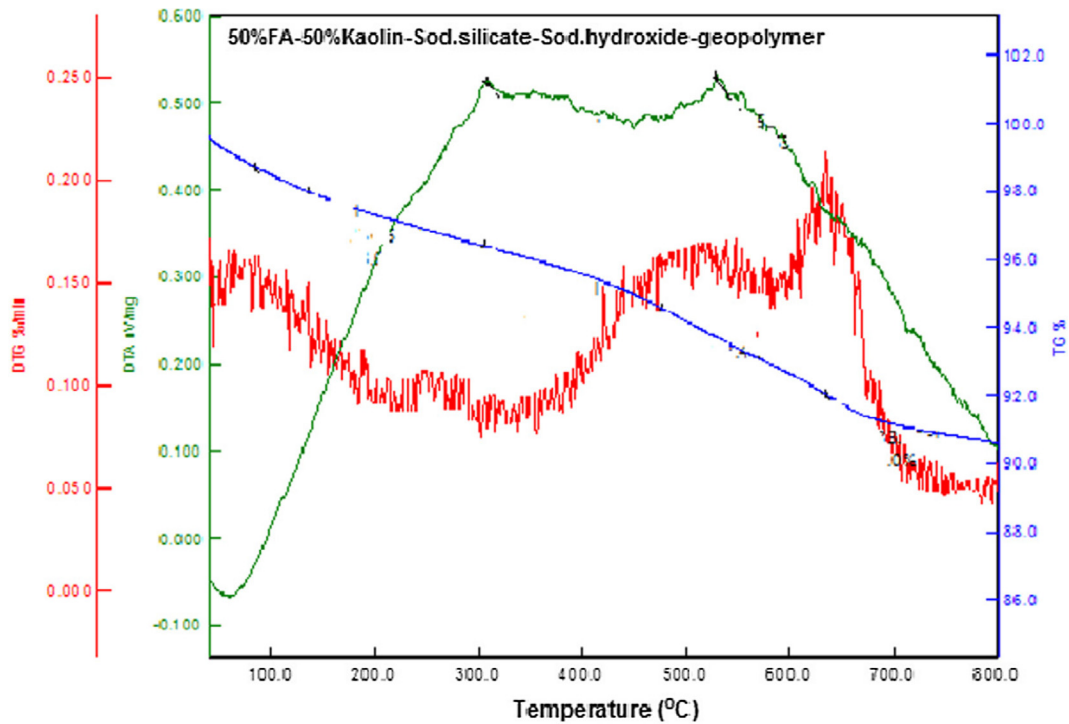


Fig. 38. TG (blue)/DTG (red)/DTA (green) curves for kaolin with fly ash-based geopolymer [36]. (For interpretation of the references to colour in this figure legend, the reader is referred to the web version of this article.)

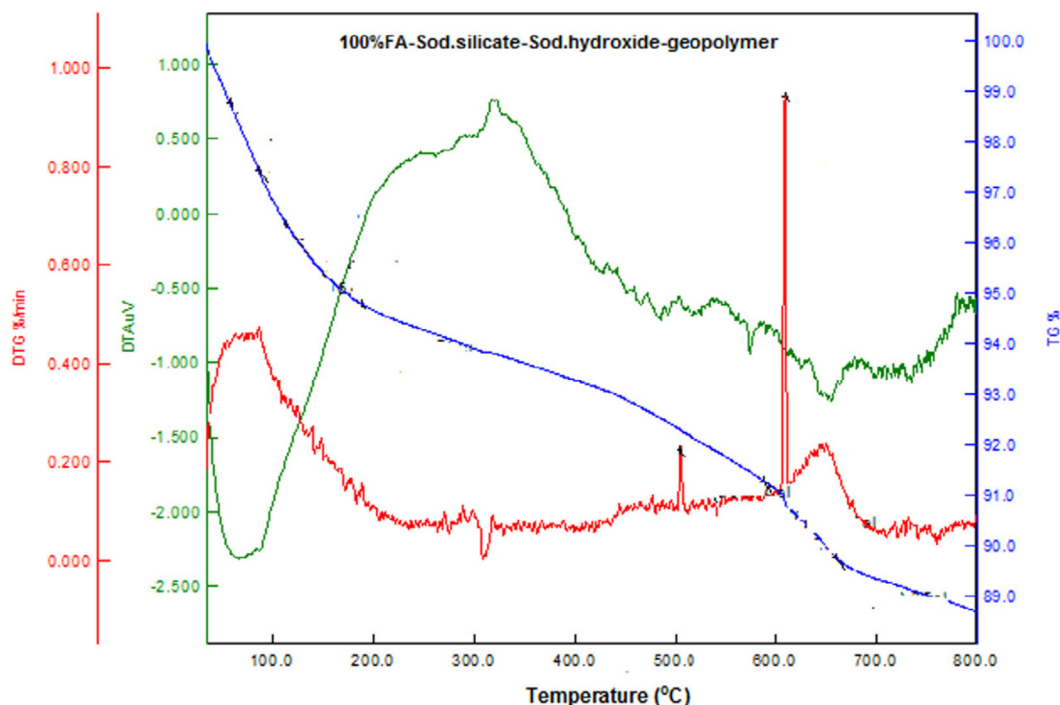


Fig. 39. TG (blue)/DTG (red)/DTA (green) curves for fly ash-based geopolymer [36]. (For interpretation of the references to colour in this figure legend, the reader is referred to the web version of this article.)

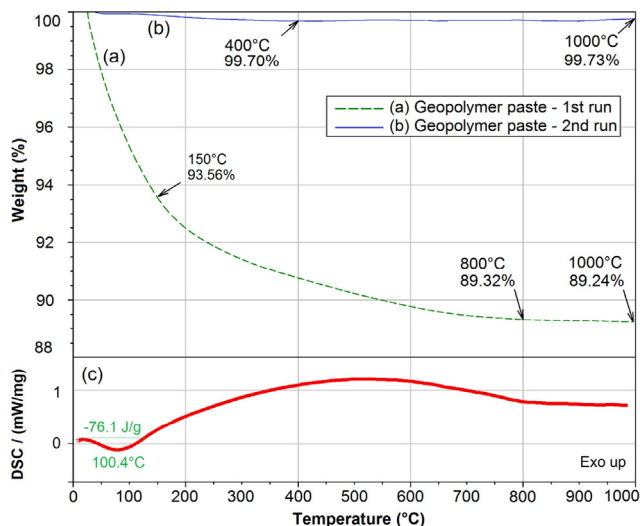


Fig. 40. TGA curves of hardened pure geopolymer during the first (a) and the second run (b) with DSC curve during the first run (c) [45].

sample (ET1). The  $\text{—Si—O—Si—}$  bending vibration was closely related with the distinctive intensity band recorded at  $445\text{ cm}^{-1}$ . Also, the  $\text{—Si—O—Si—}$  and  $\text{—Si—O—Al—}$  irregular stretching vibrations for all the materials were observed at the band of  $990\text{ cm}^{-1}$  [75,76]. The band of approximately  $990\text{ cm}^{-1}$  decreased when the POFA-to-FA ratio increased as displayed in Fig. 31. The modified mean chain length of the aluminosilicate polymers was demonstrated by the intensity alteration of the band.

According to Zhang et al. [77] the weak band observed is responsible for the bending vibration of  $\text{Si—OH}$  for FA and POFA-based geopolymer mortar. The band observed was located at approximately  $845\text{ cm}^{-1}$ . As the ratio of POFA used was increased, traces of the band growth have been recorded. For sample ET5, ET7, ET8 and mortar samples without POFA had shown no existence of the weak band. The  $\text{Si—OH}$  bond is known to lower the degree of matrix condensation which contributed to weaker mechanical properties.

In addition, the presence of Al in octahedral coordination was demonstrated by the bands at  $560\text{ cm}^{-1}$  [58,78]. On the other hand, small band recorded around  $670\text{ cm}^{-1}$  was revealed to be representing the functional group of aluminium oxide ( $\text{AlO}_2$ ) [79]. Phases of quartz were identified as crystalline at the band of approximately  $760\text{--}770\text{ cm}^{-1}$  for all the mortars tested. At roughly  $1450\text{ cm}^{-1}$ , spectra bands were observed in all the mortar samples. As a result of atmospheric carbonation of alkaline activation media, sodium carbonate might be present; where the band recorded was known for carbonate asymmetric stretching. Normally, atmospheric carbonation was shown for  $\text{O—C—O}$  stretching vibration in sodium hydroxide rich geopolymer [75]. The intensity band at  $2100\text{ cm}^{-1}$  was assigned to physically absorbed CO and H bonded CO while  $2300\text{ cm}^{-1}$  was designated for  $\text{C}\equiv\text{N}$  [80]. Apart from that, raising the ratio of FA-to-POFA was prone in increasing the bands at  $2100$  and  $2300\text{ cm}^{-1}$ . It is known that both the bands are detectable in zeolite structures too.

**3.3.3.3. Metakaolin-based geopolymer.** FTIR analysis of acid (GPS4) and alkali-based (GPWP) geopolymers are displayed in Fig. 32 [37]. The bands recorded at approximately  $449$  and  $460\text{ cm}^{-1}$  in the FTIR analysis for both geopolymer samples are assigned for the  $\text{Si—O—Si}$  in-plane vibration. FTIR analysis of MK has shown that the band at  $546\text{ cm}^{-1}$  attributed to  $\text{S—O—Al}^{\text{VI}}$  as it deviated toward a lower wavenumber at approximately  $530$  and  $536\text{ cm}^{-1}$  after the process of geopolymerization. It is predicted that the shift toward lower wavenumber recorded for acid-based geopolymer due to the incomplete replacement of  $\text{SiO}_4$  by  $\text{PO}_4$ , in which the local chemical environment was changed [81]. On the other hand, the reorganization of aluminium in 6-fold coordination after the process of geopolymerization might have caused the shift of alkali-based geopolymer sample. Formation of band at  $590\text{ cm}^{-1}$  could be due to the reorganization of aluminium. According to previous study, the absorption band recorded at  $592\text{ cm}^{-1}$  for GPWP sample attributed to the vibrations of  $\text{AlO}_6$  and the formation of berlinite [82]. Stretching of vibration modes of  $\text{Si—O—Si}$  and  $\text{Si—O—P}$  for the GPS4 was corresponding to the band at  $666\text{ cm}^{-1}$  and  $799\text{ cm}^{-1}$ , respectively [83].

For the GPWP sample, the band recorded at  $673\text{ cm}^{-1}$  ascribed to  $\text{Si—O—Si}$  which was predicted from the present of quartz. Gao et al. [72] discussed that the fundamental geopolymer structure was produced after the reaction between the silicon aluminates and alkaline solution where the absorption band for GPWP sample located at roughly  $712\text{ cm}^{-1}$  as detected in the FTIR analysis. The absorption band of  $\text{Si—O—Al}^{\text{IV}}$  might be related to the formation of geopolymer framework which was highly cross-linking [72]. This was justified through higher strength and high-density matrices recorded from the tests results. Bending vibration of  $\text{Si—OH}$  and  $\text{P—O}$  was assigned based on the band at  $865\text{ cm}^{-1}$  and  $925\text{ cm}^{-1}$ , respectively [81].

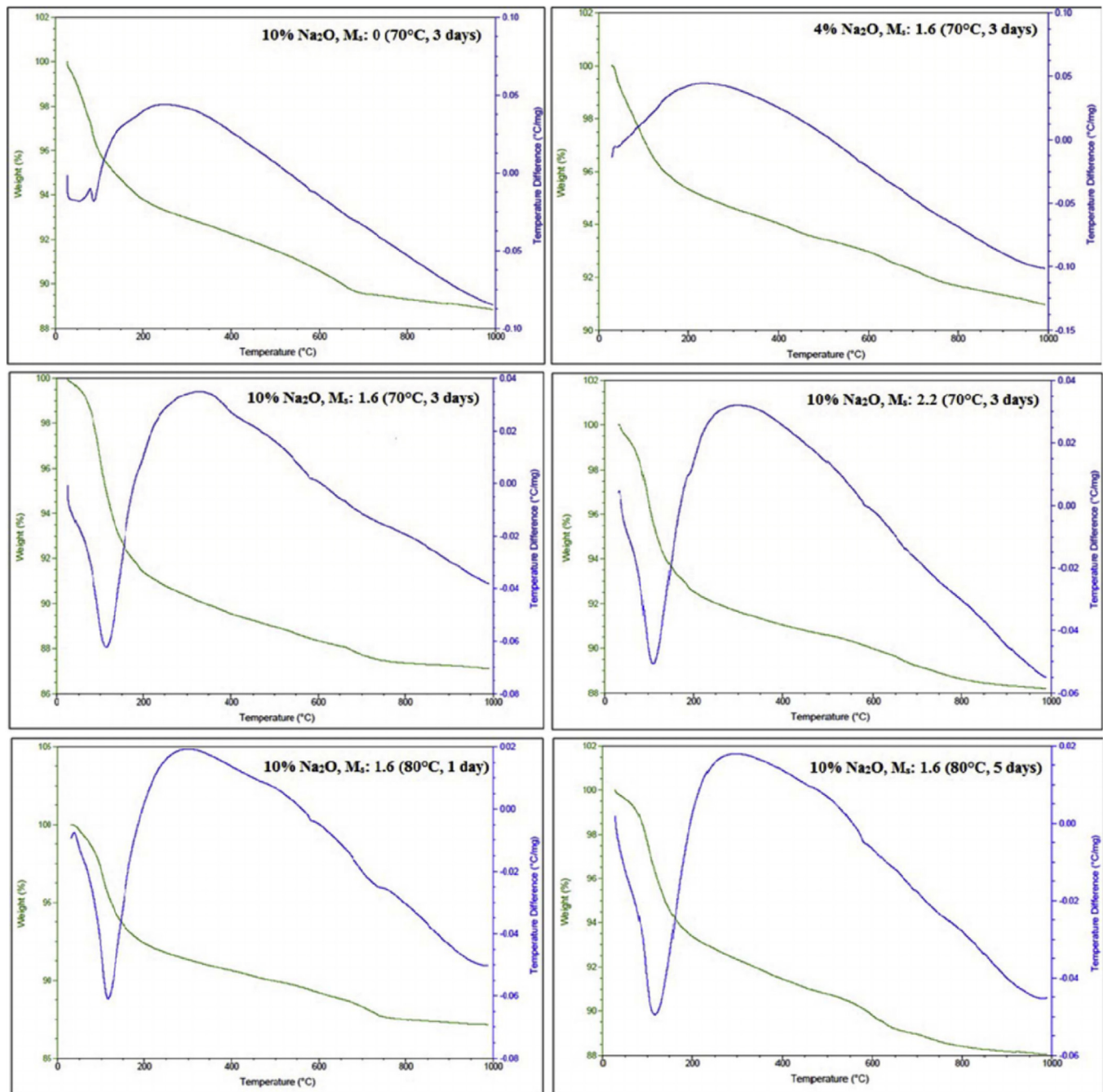


**Fig. 41.** TGA results of waste clay brick powder-based geopolymers. (a) 10% Na<sub>2</sub>O, SiO<sub>2</sub>/Na<sub>2</sub>O: 0, (b) 4% Na<sub>2</sub>O, SiO<sub>2</sub>/Na<sub>2</sub>O: 1.6, (c) 10% Na<sub>2</sub>O, SiO<sub>2</sub>/Na<sub>2</sub>O: 1.6, (d) 10% Na<sub>2</sub>O, SiO<sub>2</sub>/Na<sub>2</sub>O: 2.2 (70 °C for 3 days), (e) 10% Na<sub>2</sub>O, SiO<sub>2</sub>/Na<sub>2</sub>O: 1.6 (80 °C for 24 h) and (f) 10% Na<sub>2</sub>O, SiO<sub>2</sub>/Na<sub>2</sub>O: 1.6 (80 °C for 5 days) [48].

The comparison of Figs. 32 and 33 shows absorption band recorded at 1076  $\text{cm}^{-1}$  from the MK, the FTIR spectrum was shifted to 1088  $\text{cm}^{-1}$  in the spectrum of GPS4. On the other hand, the absorption band shifted to a lower wavenumber of 1019  $\text{cm}^{-1}$  for the GPWP sample. From the shifting of the wavenumber, it demonstrates formation of materials, different from the original MK. Both the acid and alkali mediums enabled depolymerization and polycondensation of materials in the process of geopolymerization. The shifting of wavenumber further hinted the formation of Si—O—Si—O—Al—O and Si—O—Si—O—P—O in the chain of geopolymer samples for both acidic and alkaline mediums accordingly.

The wide bands observed at roughly 1647  $\text{cm}^{-1}$  and 3420  $\text{cm}^{-1}$  correlates to the extension and deformation vibration modes of H—O—H and O—H bond. However, an absorption band at roughly 1440  $\text{cm}^{-1}$  was recorded in the analysis of alkali-based geopolymer. Presence of the band was attributed to the C—O of carbonate

groups on account of the existence of sodium ions in the nano silica fume which reacted with CO<sub>2</sub> in the atmosphere.

### 3.3.4. Thermogravimetric analysis

**3.3.4.1. Fly ash-based geopolymer.** Thermal analysis was carried out by Abdulkareem et al. [20] in order to measure the mass loss as a function of temperature from 25 °C to 800 °C. Thermogravimetric analysis (TGA) and the derivative thermogravimetric analysis (DTG) curves for the geopolymer paste were displayed in Figs. 34 and 35. Loss of water due to evaporation of both the free and some of the chemically bonded water from geopolymer was demonstrated with decrease in mass rapidly before 150 °C [20]. Roughly 55–60% of free water present in the geopolymer matrix evaporated before 100 °C in samples was illustrated by the sharp weight loss. However, it is

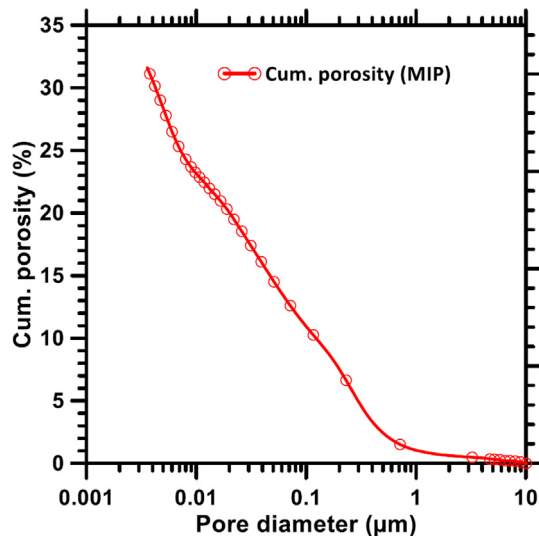


Fig. 42. Cumulative porosity-pore diameter relationship from MIP [34].

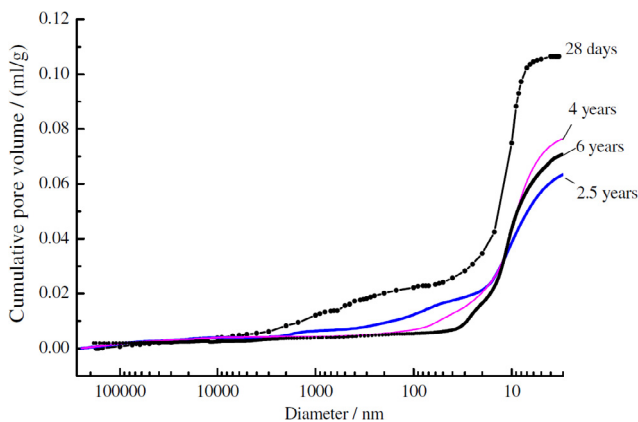


Fig. 43. Cumulative pore volume of early ages and long term slag-based geopolymer [55].

observed that the rate of weight loss stabilized from 150 °C to 780 °C, on account of the evaporation of chemically bonded water and the hydroxyl groups, OH. No further mass loss was detected with the increase of temperature to 800 °C. The average of the mass after heated to 800 °C was 79.8% as reported in Fig. 34.

Kong and Sanjayan [18] has analyzed the behavior of FA-based geopolymer paste under elevated temperature. Withstanding with Abdulkareem et al. [20], the sharp weight loss came at 250 °C instead of 150 °C, which is also attributed to the evaporation of hydroxyl group [63]. The change in weight is rather constant after 300 °C. Kong and Sanjayan [18] hypothesize that the slow rate of thermal shrinkage recorded from 300 °C and above is associated with the low rate of weight loss. The average mass recorded after 800 °C exposure was 89% (see Fig. 36).

Duan et al. [53] studied the thermal analysis of geopolymer paste with iron ore tailing (IOT) as shown in Fig. 37(a)–(d). The content of calcium hydroxide  $\text{Ca}(\text{OH})_2$  decreased when the content of IOT increased, which was attributed to the lesser mass loss compared to reference sample. It is understood that the addition of IOT contributed to the formation of calcium silicate hydrate (C–S–H) by utilizing  $\text{Ca}(\text{OH})_2$ . Nevertheless, even after 30% of IOT was added in the mix, the decomposition of  $\text{Ca}(\text{OH})_2$  recorded corresponding to the endothermic peak. It was reported that  $\text{Ca}(\text{OH})_2$  still presents as only a number of the calcium was converted into C–S–H. Similar with Abdulkareem et al. (2014), the rate of mass loss at high temperature after 800 °C was negligible for all samples [20].

Thermal analysis was conducted by Okoye et al. [36] to study the thermal stability of geopolymers. As detailed in Figs. 38 and 39, the weight loss for both kaolin incorporated FA-based geopolymer and pure FA-based geopolymer samples took place at approximately 100 °C. For the FA-based geopolymer, a rather sharp drop in weight was observed when temperature increased whereas the kaolin incorporated FA-based geopolymer has a complex curve. From the observation of both samples, the ideal curing temperature could be ranged from 80 °C to 100 °C.

**3.3.4.2. Metakaolin-based geopolymer.** Kovářik et al. [45] reported thermal behavior of pure geopolymer after the first and second run by up to 1000 °C. A sharp reduction in weight from ambient temperature to 250 °C was illustrated in Fig. 40(a). Identical with previous studies, the weight loss in samples was caused by the evaporation of free water which is tightly absorbed and trapped in small pores [84]. The continuous weight loss from 200 °C to 800 °C was attributed by the condensation of hydroxyl group; similar findings was also reported by Duan et al. [53]. As the temperature increased further from 800 °C to 1000 °C, the rate of weight loss declined and almost halted. The first run of thermal analysis proved that the main contributor of weight loss in geopolymer was due to lose of water molecules. The second run to 1000 °C on the same sample was shown in Fig. 40(b). A minor weight reduction of 0.3% recorded when the same sample was tested up to 400 °C. The loss of surface water absorbed from surroundings was the main caused for weight reduction in second run.

As shown in Fig. 40(c), with heat consumption of 76 J/g, the curve corresponded to the continuous evaporation of free water, which matched well with TGA data obtained. The broad exothermic peak from 200 °C to 800 °C also contributed by the condensation of free hydroxyl groups (silanol or aluminol group) in the geopolymer. Aluminosilicate network was formed from the reaction of two hydroxyl groups [63]. The stable region with no crystallization or phase transitions from 800 °C to 1000 °C reported by the considerable heat effect in this temperature range [57].

**3.3.4.3. Waste clay brick powder-based geopolymer.** Fig. 41 shows the thermogravimetric analysis of WCBP-based geopolymer. Tuyan et al. [48] reported that the weight loss of specimen due to different concentration of AAS and curing conditions is negligible. The weight loss in the specimen happened around 100 °C and 200 °C due to the evaporation of free water entrapped. Besides that, another wave of weight loss was recorded at 650 °C and 750 °C. Bernal et al. [85] opined that the weight loss could be attributed to the decomposition of the carbonates as a result of the atmospheric carbonation that occurs while preparing the sample for analysis [85]. Referring to Fig. 41, it is understood that WCBP-based geopolymer is rather stable upon treatment up to 1000 °C than Portland cement. Salih et al. [86] claimed that WCBP-based geopolymer might be a single-component material due to its thermal properties [86].

### 3.3.5. Mercury intrusion porosimetry

**3.3.5.1. Fly ash-based geopolymer.** Das et al. [34] investigated the dimension of pore structure of FA-based geopolymer in the range of 0.0036–10 μm using mercury intrusion porosimetry (MIP) to support the x-ray tomography (XRT) studies. As can be seen in Fig. 42, the cumulative porosity for FA geopolymer is approximately 32%. However, majority of the pores recorded in the geopolymer matrix were of 0.0036–1 μm as shown in the steep portion in Fig. 42.

**3.3.5.2. Ground granulated blast furnace slag-based geopolymer.** Ye et al. [42] reported the cumulative pore volume of slag-based geopolymer from early age to long term. The SEM analysis (Fig. 43) showed that pore size in the range of approximately 3 μm and this corresponds to large pores recorded. The increase in the pressure allows the mercury to enter into the pores and the micropores recorded at nanometer scale increased from 50 nm to 6 nm intensely. The comparison of short and long-term slag-based geopolymer specimen shows that the onset of uplift changed to nanometer scale instead of micrometer as the number of micropores decreases. It is understood that the long-term geopolymer has denser matrix which contributes to the decrease in volume of mercury intrusion. As the process of geopolymerization prolonged, increasing amount of gels were filling the cracks and pores formed in the early age. Hence, this explained the strength gain at early age to long-term specimen as the cumulative pore volume is reduced.

### 3.3.6. Micro computed tomography analysis

Tuyan et al. [48] analyzed the distribution of pores of WCBP-based geopolymers using Micro CT analysis as shown in Fig. 44. Table 4 shows the mean of pore diameter and porosity of the WCBP-based geopolymer specimens. An increment of pore diameter 33.2–53.8 μm was observed when the geopolymer mixture has 10% of  $\text{Na}_2\text{O}$  content. In addition, slight reduction on porosity from 2.02 to 1.83% was observed with increasing  $\text{SiO}_2/\text{Na}_2\text{O}$  ratio from 0 to 1.6. However, the porosity dropped significantly from 4.04 to 1.83% when the  $\text{Na}_2\text{O}$  content was increased from 4 to 10%.

The effect of extension of curing period on WCBP-based geopolymer were also studied by Tuyan et al. [48]. As shown in Fig. 44(e) and (f), a denser arrangement of geopolymer matrix was observed when the curing period was extended from 1 day to 5 days. The mean dimension of pores decreased from 59.8 μm to 40.3 μm and the porosity decreased from 2.09% to 1.53%. Thus the compressive strength of geopolymer was enhanced due to prolong curing period.

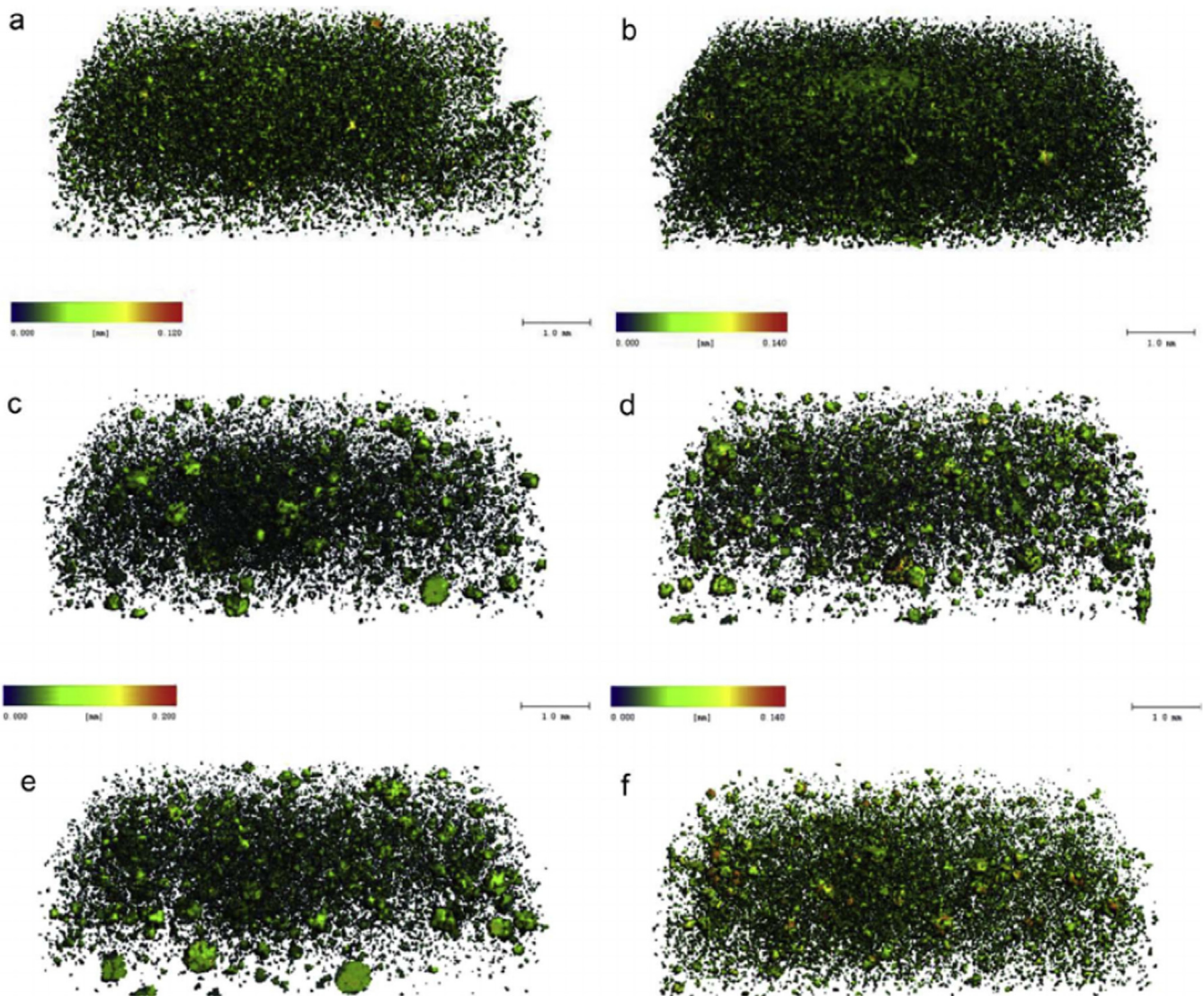


Fig. 44. Micro CT analysis of waste clay brick powder-based geopolymers [48].

**Table 4**  
Average pore diameter and porosity of waste clay brick-based geopolymers [48].

Mix	10% Na <sub>2</sub> O; SiO <sub>2</sub> /Na <sub>2</sub> O: 0 70 °C, 3 days	4% Na <sub>2</sub> O; SiO <sub>2</sub> /Na <sub>2</sub> O: 1.6 70 °C, 3 days	10% Na <sub>2</sub> O; SiO <sub>2</sub> /Na <sub>2</sub> O: 1.6 70 °C, 3 days	10% Na <sub>2</sub> O; SiO <sub>2</sub> /Na <sub>2</sub> O: 2.2 70 °C, 3 days	10% Na <sub>2</sub> O; SiO <sub>2</sub> /Na <sub>2</sub> O: 1.6 80 °C, 1 day	10% Na <sub>2</sub> O; SiO <sub>2</sub> /Na <sub>2</sub> O: 1.6 80 °C, 5 days
Average pore diameter (μm)	33.2	36.9	53.8	53.8	59.8	40.3
Porosity (%) (Micro CT)	2.02	4.04	1.83	1.94	2.09	1.53

#### 4. Conclusion

Based on the review of geopolymer mixes that were investigated for microstructural behavior with relation to their compressive strength, some important conclusions were drawn. The presence of macropores and cracks at the early stage in the geopolymer mixes is one of the main reasons for weak matrix and strength gain. It can be generalized that geopolymers with 12 M of sodium hydroxide solution, low liquid-to-binder ratio of about 0.4 and curing temperature at approximately 70 °C for at least 24 h produced high strength geopolymers. Incorporation of

nanomaterial might serve as filler and or, to enhance the process of geopolymerization. Addition of nano materials such as nano silica and nano alumina in binder with low pozzolanic oxide content is important to form Si—O—Al—O bond. Based on the SEM images, binders mixed with lower mass ratio of SS/SH from 2.0 to 2.5 tend to react more efficiently due to high surface area to react and bind without being blocked by the presence of extra water. However, hydroxyl groups tend to condense when the specimens undergo high temperature. Based on TGA analysis, the evaporation of free water molecule is the main factor that causes weight loss in the specimen. The investigation through MIP and Micro CT analysis

shows the extension of curing period of geopolymer specimen is an alternative to enhance the production of geopolymer gel which in turn is effective in reducing the pores. The enhancement of geopolymerization block the link between the pores and thus resulting in denser arrangement.

### Conflict of interest

None.

### Acknowledgments

The authors gratefully acknowledge the funding provided by University of Malaya through University of Malaya, Grand Challenge – SUS (Sustainability Science) Grant, project number GC003A-15SUS – Development of Effective Repair and Rehabilitation Material Consisting Local Waste Materials for Affordable Housing.

### References

- [1] J.W. Vermuelen, Tony, Biodiversity and cultural property in the management of limestone resources - lessons from East Asia, Washington D.C., 1999.
- [2] M. Alnahhal et al., Evaluation of industrial by-products as sustainable pozzolanic materials in recycled aggregate concrete, *Sustainability* 9 (5) (2017) 767.
- [3] M. Schneider et al., Sustainable cement production—present and future, *Cem. Concr. Res.* 41 (7) (2011) 642–650.
- [4] E. Benhelal et al., Global strategies and potentials to curb CO<sub>2</sub> emissions in cement industry, *J. Cleaner Prod.* 51 (2013) 142–161.
- [5] D. Department of Statistic, Malaysia Cement Production, 2016 (15th June, 2017). Available from: <<http://www.dosm.gov.my/v1/>>.
- [6] Y. Kim, K. Kim, G.-Y. Jeong, Study of detailed geochemistry of hazardous elements in weathered coal ashes, *Fuel* 193 (2017) 343–350.
- [7] L. Assi et al., Improvement of the early and final compressive strength of fly ash-based geopolymer concrete at ambient conditions, *Constr. Build. Mater.* 123 (2016) 806–813.
- [8] P. Duan et al., Fresh properties, compressive strength and microstructure of fly ash geopolymer paste blended with iron ore tailing under thermal cycle, *Constr. Build. Mater.* 118 (2016) 76–88.
- [9] P. Duan et al., An investigation of the microstructure and durability of a fluidized bed fly ash–metakaolin geopolymer after heat and acid exposure, *Mater. Des.* 74 (2015) 125–137.
- [10] F.N. Okoye, J. Durgaprasad, N.B. Singh, Effect of silica fume on the mechanical properties of fly ash based-geopolymer concrete, *Ceram. Int.* 42 (2) (2016) 3000–3006.
- [11] P. Pavithra et al., A mix design procedure for geopolymer concrete with fly ash, *J. Cleaner Prod.* 133 (2016) 117–125.
- [12] S. Andrejkovičová et al., The effect of natural zeolite on microstructure, mechanical and heavy metals adsorption properties of metakaolin based geopolymers, *Appl. Clay Sci.* 126 (2016) 141–152.
- [13] V.D. Cao et al., Microencapsulated phase change materials for enhancing the thermal performance of Portland cement concrete and geopolymer concrete for passive building applications, *Energy Convers. Manage.* 133 (2017) 56–66.
- [14] B.C. McLellan et al., Costs and carbon emissions for geopolymer pastes in comparison to ordinary Portland cement, *J. Cleaner Prod.* 19 (9) (2011) 1080–1090.
- [15] R.G. Bligh, Tom, Development of geopolymer precast floor panels for the Global Change Institute at University of Queensland, in: Australasian Structural Engineering (ASEC) Conference 2014, Auckland, New Zealand, 2014.
- [16] J. Davidovits, Geopolymers, *J. Therm. Anal.* 37 (8) (1991) 1633–1656.
- [17] J. Davidovits, Properties of geopolymer cement, First International Conference on Alkaline Cements and Concretes, Kiev State Technical University: Vipol Stock Company, 1994.
- [18] D.L.Y. Kong, J.G. Sanjayan, Effect of elevated temperatures on geopolymer paste, mortar and concrete, *Cem. Concr. Res.* 40 (2) (2010) 334–339.
- [19] T. Xie, T. Ozbakkaloglu, Behavior of low-calcium fly and bottom ash-based geopolymer concrete cured at ambient temperature, *Ceram. Int.* 41 (4) (2015) 5945–5958.
- [20] O.A. Abdulkareem et al., Effects of elevated temperatures on the thermal behavior and mechanical performance of fly ash geopolymer paste, mortar and lightweight concrete, *Constr. Build. Mater.* 50 (2014) 377–387.
- [21] R. Embong et al., Strength and microstructural properties of fly ash based geopolymer concrete containing high-calcium and water-absorptive aggregate, *J. Cleaner Prod.* 112 (2016) 816–822.
- [22] D. Adak, M. Sarkar, S. Mandal, Structural performance of nano-silica modified fly-ash based geopolymer concrete, *Constr. Build. Mater.* 135 (2017) 430–439.
- [23] P. Duan et al., Effects of adding nano-TiO<sub>2</sub> on compressive strength, drying shrinkage, carbonation and microstructure of fluidized bed fly ash based geopolymer paste, *Constr. Build. Mater.* 106 (2016) 115–125.
- [24] N. Ranjbar et al., Compressive strength and microstructural analysis of fly ash/palm oil fuel ash based geopolymer mortar under elevated temperatures, *Constr. Build. Mater.* 65 (2014) 114–121.
- [25] M.Y.J. Liu et al., Microstructural investigations of palm oil fuel ash and fly ash based binders in lightweight aggregate foamed geopolymer concrete, *Constr. Build. Mater.* 120 (2016) 112–122.
- [26] Y. Park et al., Compressive strength of fly ash-based geopolymer concrete with crumb rubber partially replacing sand, *Constr. Build. Mater.* 118 (2016) 43–51.
- [27] M.S.H. Khan et al., Utilisation of steel furnace slag coarse aggregate in a low calcium fly ash geopolymer concrete, *Cem. Concr. Res.* 89 (2016) 220–229.
- [28] H. Assaedi, F.U.A. Shaikh, I.M. Low, Influence of mixing methods of nano silica on the microstructural and mechanical properties of flax fabric reinforced geopolymer composites, *Constr. Build. Mater.* 123 (2016) 541–552.
- [29] C. Gunasekara, D.W. Law, S. Setunge, Long term permeation properties of different fly ash geopolymer concretes, *Constr. Build. Mater.* 124 (2016) 352–362.
- [30] H.Y. Leong et al., Suitability of Sarawak and Gladstone fly ash to produce geopolymers: a physical, chemical, mechanical, mineralogical and microstructural analysis, *Ceram. Int.* 42 (8) (2016) 9613–9620.
- [31] D.M.A. Huiskes et al., Design and performance evaluation of ultra-lightweight geopolymer concrete, *Mater. Des.* 89 (2016) 516–526.
- [32] S. Zeng, J. Wang, Characterization of mechanical and electric properties of geopolymers synthesized using four locally available fly ashes, *Constr. Build. Mater.* 121 (2016) 386–399.
- [33] T. Tho-In et al., Compressive strength and microstructure analysis of geopolymer paste using waste glass powder and fly ash, *J. Cleaner Prod.* 172 (2018) 2892–2898.
- [34] S. Das et al., Effective properties of a fly ash geopolymer: Synergistic application of X-ray synchrotron tomography, nanoindentation, and homogenization models, *Cem. Concr. Res.* 78 (2015) 252–262.
- [35] S. Pilehvar et al., Physical and mechanical properties of fly ash and slag geopolymer concrete containing different types of micro-encapsulated phase change materials, *Constr. Build. Mater.* 173 (2018) 28–39.
- [36] F.N. Okoye, J. Durgaprasad, N.B. Singh, Mechanical properties of alkali activated flyash/kaolin based geopolymer concrete, *Constr. Build. Mater.* 98 (2015) 685–691.
- [37] H.K. Tchakouté, C.H. Rüscher, Mechanical and microstructural properties of metakaolin-based geopolymer cements from sodium waterglass and phosphoric acid solution as hardeners: a comparative study, *Appl. Clay Sci.* 140 (2017) 81–87.
- [38] A. Noushini et al., Compressive stress-strain model for low-calcium fly ash-based geopolymer and heat-cured Portland cement concrete, *Cem. Concr. Compos.* 73 (2016) 136–146.
- [39] N. Ranjbar et al., Compressive strength and microstructural analysis of fly ash/palm oil fuel ash based geopolymer mortar, *Mater. Des.* 59 (2014) 532–539.
- [40] S.M.A. Kabir et al., Performance evaluation and some durability characteristics of environmental friendly palm oil clinker based geopolymer concrete, *J. Cleaner Prod.* 161 (2017) 477–492.
- [41] A.S.M. Abdul Awal, M. Warid Hussin, Effect of palm oil fuel ash in controlling heat of hydration of concrete, *Proc. Eng.* 14 (2011) 2650–2657.
- [42] J. Ye, W. Zhang, D. Shi, Properties of an aged geopolymer synthesized from calcined ore-dressing tailing of bauxite and slag, *Cem. Concr. Res.* 100 (Suppl. C) (2017) 23–31.
- [43] B. Yan, P. Duan, D. Ren, Mechanical strength, surface abrasion resistance and microstructure of fly ash–metakaolin–sepiolite geopolymer composites, *Ceram. Int.* 43 (1, Part B) (2017) 1052–1060.
- [44] A. Sharmin et al., Influence of source materials and the role of oxide composition on the performance of ternary blended sustainable geopolymer mortar, *Constr. Build. Mater.* 144 (2017) 608–623.
- [45] T. Kovářik et al., Thermomechanical properties of particle-reinforced geopolymer composite with various aggregate gradation of fine ceramic filler, *Constr. Build. Mater.* 143 (2017) 599–606.
- [46] J.N. Yankwa Djobo et al., Mechanical properties and durability of volcanic ash based geopolymer mortars, *Constr. Build. Mater.* 124 (2016) 606–614.
- [47] E. Nimwinya et al., A sustainable calcined water treatment sludge and rice husk ash geopolymer, *J. Cleaner Prod.* 119 (2016) 128–134.
- [48] M. Tuyan, Ö. Andiç-Çakir, K. Ramyar, Effect of alkali activator concentration and curing condition on strength and microstructure of waste clay brick powder-based geopolymer, *Compos. B Eng.* 135 (2018) 242–252.
- [49] O.A.R. Abdulkareem, Mahyuddin, Optimization of alkaline activator mixing and curing conditions for a fly ash-based geopolymer paste system, *Mod. Appl. Sci.* 9 (12) (2015) 61–69.
- [50] M. Soutsos et al., Factors influencing the compressive strength of fly ash based geopolymers, *Constr. Build. Mater.* 110 (Suppl. C) (2016) 355–368.
- [51] O.A. Abdulkareem, M. Ramli, Optimization of alkaline activator mixing and curing conditions for a fly ash-based geopolymer paste system, *Mod. Appl. Sci.* 9 (12) (2015) 61.
- [52] T. Bakharev, Geopolymeric materials prepared using Class F fly ash and elevated temperature curing, *Cem. Concr. Res.* 35 (6) (2005) 1224–1232.
- [53] P. Duan et al., Fresh properties, mechanical strength and microstructure of fly ash geopolymer paste reinforced with sawdust, *Constr. Build. Mater.* 111 (2016) 600–610.

- [54] K. Korniejenco et al., Mechanical properties of geopolymer composites reinforced with natural fibers, *Proc. Eng.* 151 (Suppl. C) (2016) 388–393.
- [55] N. Ranjbar et al., High tensile strength fly ash based geopolymer composite using copper coated micro steel fiber, *Constr. Build. Mater.* 112 (2016) 629–638.
- [56] I.I. Bashar et al., Engineering properties and fracture behaviour of high volume palm oil fuel ash based fibre reinforced geopolymer concrete, *Constr. Build. Mater.* 111 (2016) 286–297.
- [57] P. He et al., Thermal evolution and crystallization kinetics of potassium-based geopolymer, *Ceram. Int.* 37 (1) (2011) 59–63.
- [58] A. Palomo, M.W. Grutzeck, M.T. Blanco, Alkali-activated fly ashes: a cement for the future, *Cem. Concr. Res.* 29 (8) (1999) 1323–1329.
- [59] C. Villa et al., Geopolymer synthesis using alkaline activation of natural zeolite, *Constr. Build. Mater.* 24 (11) (2010) 2084–2090.
- [60] P. Chindapasirt, T. Chareerat, V. Sirivivatnanon, Workability and strength of coarse high calcium fly ash geopolymer, *Cem. Concr. Compos.* 29 (3) (2007) 224–229.
- [61] N.W. Chen-Tan et al., Determining the reactivity of a fly ash for production of geopolymer, *J. Am. Ceram. Soc.* 92 (4) (2009) 881–887.
- [62] P. Chindapasirt et al., Comparative study on the characteristics of fly ash and bottom ash geopolymers, *Waste Manage. (Oxford)* 29 (2) (2009) 539–543.
- [63] P. Duxson et al., Effect of alkali cations on aluminum incorporation in geopolymeric gels, *Ind. Eng. Chem. Res.* 44 (4) (2005) 832–839.
- [64] T. Phoo-ngernkham et al., The effect of adding nano-SiO<sub>2</sub> and nano-Al<sub>2</sub>O<sub>3</sub> on properties of high calcium fly ash geopolymer cured at ambient temperature, *Mater. Des.* 55 (2014) 58–65.
- [65] A. Wongsu et al., Use of municipal solid waste incinerator (MSWI) bottom ash in high calcium fly ash geopolymer matrix, *J. Cleaner Prod.* 148 (2017) 49–59.
- [66] Y.S. Zhang, W. Sun, Z.J. Li, Hydration process of potassium polysialate (K-PSDS) geopolymer cement, *Adv. Cem. Res.* 17 (1) (2005) 23–28.
- [67] M.A. Salih, A.A. Abang Ali, N. Farzadnia, Characterization of mechanical and microstructural properties of palm oil fuel ash geopolymer cement paste, *Constr. Build. Mater.* 65 (2014) 592–603.
- [68] J.C. Swanepoel, C.A. Strydom, Utilisation of fly ash in a geopolymeric material, *Appl. Geochem.* 17 (8) (2002) 1143–1148.
- [69] A. Fernández-Jiménez, A. Palomo, Composition and microstructure of alkali activated fly ash binder: effect of the activator, *Cem. Concr. Res.* 35 (10) (2005) 1984–1992.
- [70] S. Andini et al., Coal fly ash as raw material for the manufacture of geopolymer-based products, *Waste Manage. (Oxford)* 28 (2) (2008) 416–423.
- [71] D. Panias, I.P. Giannopoulou, T. Perraki, Effect of synthesis parameters on the mechanical properties of fly ash-based geopolymers, *Colloids Surf. A: Physicochem. Eng. Asp.* 301 (1) (2007) 246–254.
- [72] K. Gao et al., Effects SiO<sub>2</sub>/Na<sub>2</sub>O molar ratio on mechanical properties and the microstructure of nano-SiO<sub>2</sub> metakaolin-based geopolymers, *Constr. Build. Mater.* 53 (2014) 503–510.
- [73] M.R. Karim et al., Fabrication of a non-cement binder using slag, palm oil fuel ash and rice husk ash with sodium hydroxide, *Constr. Build. Mater.* 49 (2013) 894–902.
- [74] M.F. Zawrah et al., Recycling and utilization assessment of waste fired clay bricks (Grog) with granulated blast-furnace slag for geopolymer production, *Process Saf. Environ. Prot.* 103 (2016) 237–251.
- [75] W.K.W. Lee, J.S.J. van Deventer, The effects of inorganic salt contamination on the strength and durability of geopolymers, *Colloids Surf. A: Physicochem. Eng. Asp.* 211 (2) (2002) 115–126.
- [76] K. Somna et al., NaOH-activated ground fly ash geopolymer cured at ambient temperature, *Fuel* 90 (6) (2011) 2118–2124.
- [77] Z. Yunsheng, S. Wei, L. Zongjin, Composition design and microstructural characterization of calcined kaolin-based geopolymer cement, *Appl. Clay Sci.* 47 (3) (2010) 271–275.
- [78] Q. Li et al., Synthesis of geopolymer composites from blends of CFBC fly and bottom ashes, *Fuel* 97 (2012) 366–372.
- [79] K. Komnitsas, D. Zaharaki, V. Perdikatsis, Geopolymerisation of low calcium ferronickel slags, *J. Mater. Sci.* 42 (9) (2007) 3073–3082.
- [80] K. Chakarova, K. Hadjiivanov, Problems in the IR measuring the acidity of zeolite bridging hydroxyls by low-temperature CO adsorption, *Chem. Commun.* 47 (6) (2011) 1878–1880.
- [81] S. Louati et al., Structure and properties of new eco-material obtained by phosphoric acid attack of natural Tunisian clay, *Appl. Clay Sci.* 101 (2014) 60–67.
- [82] W.R. Taylor, Application of infrared spectroscopy to studies of silicate glass structure: examples from the melilite glasses and the systems Na<sub>2</sub>O-SiO<sub>2</sub> and Na<sub>2</sub>O-Al<sub>2</sub>O<sub>3</sub>-SiO<sub>2</sub>, *Proc. Indian Acad. Sci. - Earth Planet. Sci.* 99 (1) (1990) 99–117.
- [83] L. Stoch, M. Środa, Infrared spectroscopy in the investigation of oxide glasses structure, *J. Mol. Struct.* 511 (1999) 77–84.
- [84] J.L. Bell, P.E. Driemeyer, W.M. Kriven, Formation of ceramics from metakaolin-based geopolymers: Part I—Cs-based geopolymer, *J. Am. Ceram. Soc.* 92 (1) (2009) 1–8.
- [85] S.A. Bernal et al., Effect of silicate modulus and metakaolin incorporation on the carbonation of alkali silicate-activated slags, *Cem. Concr. Res.* 40 (6) (2010) 898–907.
- [86] M.A. Salih et al., Effect of different curing temperatures on alkali activated palm oil fuel ash paste, *Constr. Build. Mater.* 94 (2015) 116–125.